Analysis of Aero-Optical Jitter in Convective Turbulent Flows Using Stitching Method

Matthew R. Kemnetz*
U.S. Air Force Research Laboratory, Kirtland Air Force Base, New Mexico 87117
and
Stanislav Gordeyev†
University of Notre Dame, Notre Dame, Indiana 46556

https://doi.org/10.2514/1.J060756

In the typical analysis of aero-optical wave-front data, the three lowest-order spatial modes (namely, unsteady piston as well as X and Y tilts) are removed from the experimentally measured wave fronts. These modes are commonly corrupted by mechanical disturbances. In this work, an algorithm called the stitching method was developed that takes advantage of the advective nature of the optical aberrations caused by turbulent structures to recover the unsteady global X-tilt and piston modes from experimental time-resolved wave fronts. One-dimensional modeling and related uncertainty analysis showed that for the wave fronts collected with sufficient sampling frequency, the algorithm is able to correctly recover the aero-optical component of the unsteady X tilt. In this manner, the time series of true wave fronts can be recovered. To further validate the stitching method, spatiotemporal wave-front measurements were conducted on a Mach 0.6/0.1 forced shear layer. The predicted results for the rms of the aero-optical X tilt from the stitching method agree well with the modeled results. Since the stitching method recovers the time series of the aero-optical global X tilt, the global tilt spectra were also computed and presented. This information can be used by system designers to specify the requirements for adaptive-optics system components, such as fast steering mirrors in airborne directed energy systems.

Nomenclature

A, B	=	global X- and Y-tilt components
Ap	=	aperture size in the streamwise direction
Ap_z	=	aperture size in the spanwise direction
a	=	speed of sound
C	=	piston component
Corr	=	correlation function
D_1, D_2, D_3	=	coefficients
E	=	optic field
F	=	focal length
f	=	frequency
f_f	=	forcing frequency
f_s	=	sampling frequency
G_A	=	global jitter transfer function, defined in Eq. (18)
K_{GD}	=	Gladstone–Dale constant
k_x	=	$2\pi/\Lambda$
L	=	distance of beam propagation
L_{Overlap}	=	streamwise extent of overlap region
M	=	Mach number
N_p	=	number of spatial points in streamwise direction
n	=	index of refraction
Overlap	=	relative overlap parameter
S_G	=	global tilt autocorrelation spectral density
S_θ	=	deflection angle autocorrelation spectral density
St_{Ap}	=	$(fAp)/U_c$
St_Λ	=	$(f\Lambda)/U_c$
t	=	time
U	=	function, defined in Eq. (14)
W	=	higher-order apertured wave front
$\tilde{W}_{\mathrm{true}}$	=	true wave front
$\tilde{W}$	=	true apertured wave front
x	=	streamwise coordinate
y	=	wall-normal coordinate
Z	=	Ap/Λ
z	=	spanwise coordinate
Δx	=	streamwise shift
Δz	=	spanwise shift
ϵ	=	Gaussian noise level
θ	=	deflection angle
θ_G	=	global tilt in streamwise direction
Λ	=	shear-layer streamwise structure size
λ	=	laser wavelength
ρ	=	fluid density
ρ_W	=	unbiased cross correlation
ρ_∞	=	freestream density
Σ	=	error in global tilt
$\langle\rangle$	=	spatial averaging

Subscripts

c	=	convective
rms	=	root mean square
1	=	high speed
2	=	low speed
∞	=	freestream

Superscripts

stitch	=	stitched
$'$	=	fluctuating component

Received 29 March 2021; revision received 6 June 2021; accepted for publication 8 June 2021; published online Open Access 23 September 2021.

*Research Aerospace Engineer, Directed Energy Directorate. Member AIAA.

†Associate Professor, Hessert Laboratory for Aerospace Research, Department of Mechanical and Aerospace Engineering. Associate Fellow AIAA.

I. Introduction

AIRBORNE laser systems have many applications including, but not limited to, air-to-air and air-to-ground communications, strategic missile defense, counter-unmanned-aerial-vehicle missions, and aircraft self-protect defense. For an aircraft in flight, the turbulent flow around the aircraft creates a complex unsteady density field. This complex unsteady density field distorts the index of refraction near the aircraft. The high-frequency index of refraction distortions impart

aberrations onto the outgoing laser beam, which can severely reduce its maximum intensity on the target. This reduction in intensity on the target will undoubtedly degrade system performance for communication and defense applications. The problem outlined earlier in this paragraph is the so-called aero-optics problem [1–3].

The flowfield around the aircraft not only impacts the instantaneous energy distribution on target but also degrades the effective pointing of the beam. The unintentional high-frequency pointing of the beam, or jitter, is sourced from three components. The component of jitter caused by the flow structures on the order of the aperture size is called the aero-optical jitter. The component of the jitter caused by either the unsteady motion of the platform itself or by the vibrations in the beam director induced by the platform motion is called the base motion-related jitter. Finally, the component of the jitter caused by unsteady pressure field forcing the beam director is called the aero-mechanical jitter. In a time-averaged sense, jitter enlarges the effective spot size on the target, and therefore significantly impacts on target irradiance. To improve system performance, beam jitter must be understood and eventually compensated for.

For airborne laser systems, mechanical disturbances will result in the introduction of additional unsteady X/Y tilt onto the outgoing beam. As a result, unsteady aero-optical jitter, which is a property of the flow, is almost always corrupted by the mechanical disturbances, making it difficult to measure directly. In addition, the far-field irradiance pattern depends only on the statistics of the higher-order X/Y-tilt-removed wave fronts. Therefore, the overall instantaneous X/Y tilt, which includes both the aero-optical and mechanical jitter, is typically removed from the measured wave fronts. When this necessary step is taken, information pertaining to large-scale optical structures is lost.

Adaptive-optics systems have been developed that are able to compensate for a significant portion of the mechanical jitter. An optical inertial reference unit in conjunction with a fast steering mirror and an appropriate controller can reject mechanical jitter disturbances up to 1 kHz [4,5]. Even if the jitter rejection system were to operate such that all mechanical jitter could be compensated for, the aero-optical jitter would remain. This aero-optical jitter will affect the time-averaged far-field irradiance pattern. Therefore, it is desirable to not only quantify the overall jitter of the system but to develop a method that can decouple aero-optical and mechanical jitter for additional studies.

As mentioned earlier in this paper, due to the typical processing of wave-front experimental data, all information pertaining to the aero-optical component of the jitter is removed and lost. In this work, a new algorithm is presented that takes advantage of the advective nature of aberrations to recover the time-dependent X/Y tilt, as well as piston modes, initially removed from experimentally measured wave fronts. It will be demonstrated that this algorithm enables the aero-optical component of jitter to be quantified, and information pertaining to the large-scale structures of the flow can be regained.

The aero-optics problem arises when an optical wave front encounters a turbulent time-varying flowfield. The wave front is aberrated due to the changes of index of refraction associated with the variable density flowfield. The aero-optics problem is depicted graphically in Fig. 1.

The index of refraction of a fluid varies with density as per the Gladstone–Dale relation [6,7]:

$$n(x, y, z, t) = 1 + K_{\mathrm{GD}}(\lambda)\rho(x, y, z, t) \tag{1}$$

The frame of reference is typically chosen with the z axis in the direction of the beam propagation and the x–y plane normal to it, with the origin at the center of the aperture. In Eq. (1), $K_{\mathrm{GD}}(\lambda)$ is the Gladstone–Dale constant for a given wavelength λ. In a turbulent flow, the density field ρ is a function of both space and time. Therefore, the index of refraction n is a function of not only space but also time. As a planar incident wave front propagates through this spatiotemporally varying index of the refraction field, the phase velocity of the light will be perturbed. This causes constructive and destructive interferences, as well as an overall distorted beam in the far field. This interaction of light with turbulent aerodynamic flows that causes a degradation in system performance is called the aero-optics problem.

Using Maxwell equations and a paraxial approximation, it is straightforward to show [2] that after propagating through a region of spatially–temporally changing index of refraction along the z direction, only the phase of the optic wave will be distorted, with the amount of the phase distortion equal to

$$-(2\pi/\lambda)\int_{z=0}^{z=L} n(x, y, z, t)\,\mathrm{d}z$$

The integral in this expression is called the optical path length, or OPL:

$$\mathrm{OPL}(x, y, t) = \int_{z=0}^{z=L} n(x, y, z, t)\,\mathrm{d}z \tag{2}$$

In practice, only the relative difference in the OPL over the beam aperture is important: the so-called optical path difference (OPD), $\mathrm{OPD}(x, y, t) = \mathrm{OPL}(x, y, t) - \langle \mathrm{OPL}(x, y, t)\rangle$, where the angle brackets indicate the spatial averaging over the beam aperture. Finally, the true wave front can be very closely approximated as simply a negative of the OPD: $\tilde{W}_{\mathrm{true}}(x, y, t) = -\mathrm{OPD}(x, y, t)$ [8].

The true wave front is a property of the turbulent field with a typically unbounded index of the refraction field: $n(x, y, z, t)$. However, as the intensity of the laser beam is nonzero only over a finite aperture S, only a spatially limited portion of the true wave front over the aperture (often called an apertured wave front) of $\tilde{W}(x, y, t) =$

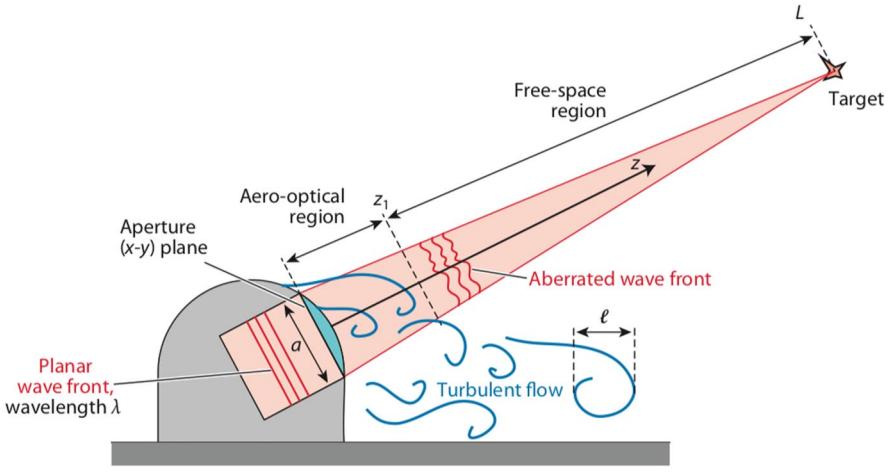

Fig. 1 Schematic of the aero-optics problem. The origin is at the center of the aperture. Reproduced with permission from the work of Wang et al. [2].

$\tilde{W}_{\text{true}}(x, y, t), (x, y) \in S$ is needed to be known. Furthermore, it is convenient at every moment in time to split the time-varying apertured wave front into a piston or spatially uniform component $C(t)$, an X/Y tilt or linear component $A(t)x + B(t)y$, and a residual or a higher-order component $W(x, y, t)$:

$$\tilde{W}(x, y, t) = C(t) + A(t)x + B(t)y + W(x, y, t) \tag{3}$$

The terms in Eq. (3) affect the far-field pattern in different ways. To investigate this, let us consider a far-field pattern of a distorted laser beam, with a constant intensity of unity across the aperture. For this beam, the initial optic field is given as $E(x, y, t) = \exp(2\pi i\tilde{W}(x, y, t)/\lambda)$. The far-field intensity is given by Fourier optics equations [9]:

$$E(x', y', t) = \frac{1}{i\lambda F}\int_S E(x, y, t)\exp\left(-2\,\pi\mathrm{i}\frac{xx' + yy'}{\lambda F}\right)\mathrm{d}x\,\mathrm{d}y \tag{4}$$

where x' and y' are the spatial coordinates at far-field plane, and F is the focal length of the lens used to generate the far-field pattern. Substituting the initial optic field into Eq. (4) and using Eq. (3), it is possible to derive the following equation for the optic field in the far field:

$$E(x', y', t) = \frac{1}{i\lambda F}\exp\left(\frac{2\pi iC(t)}{\lambda}\right)\int_S \exp\left(\frac{2\pi iW(x, y, t)}{\lambda}\right) \times \exp\left(-2\pi i\frac{x[x' - A(t)F] + y[y' - B(t)F]}{\lambda F}\right)\mathrm{d}x\,\mathrm{d}y \tag{5}$$

The intensity distribution is the square of the amplitude of $E(x', y', t)$. From Eq. (5), it is clear that the piston term $C(t)$ does not affect the far-field intensity at all. The unsteady X/Y-tilt terms do not change the far-field shape of the beam but simply cause the whole intensity pattern to move to a different location of $(x', y') = (A(t)F, B(t)F)$. Only the higher-order term, $W(x, y, t)$, affects the far-field spatial distribution, potentially decreasing the peak intensity on the target.

Explicit expressions for the unsteady X/Y-tilt terms, $A(t)$ and $B(t)$, depend on the definition of unsteady tilt. In this work, we implement the so-called Z-tilt definition [10,11]. The Z tilt is defined by the minimization of the wave front's L^2 norm in the least-squares sense over the aperture area S at each time instant:

$$\min_{A,B,C}\|W(x, y, t)\|_2 = \int_S \{\tilde{W}(x, y, t) - [C(t) + A(t)x + B(t)y]\}^2\,\mathrm{d}x\,\mathrm{d}y \tag{6}$$

This equation can be solved by forcing the partial derivatives of the integral with respect to A, B, and C to be zero, resulting in a linear system of equations for A, B, and C [8]:

$$\begin{bmatrix} \int_S \mathrm{d}x\,\mathrm{d}y & \int_S x\,\mathrm{d}x\,\mathrm{d}y & \int_S \mathrm{ydxdy} \\ \int_S x\,\mathrm{dxdy} & \int_S x^2\,\mathrm{d}x\,\mathrm{d}y & \int_S xy\,\mathrm{d}x\,\mathrm{d}y \\ \int_S y\,\mathrm{d}x\,\mathrm{d}y & \int_S xy\,\mathrm{d}x\,\mathrm{d}y & \int_S y^2\,\mathrm{d}x\,\mathrm{d}y \end{bmatrix}\begin{bmatrix} C(t) \\ A(t) \\ B(t) \end{bmatrix} = \begin{bmatrix} \int_S \tilde{W}(x, y, t)\,\mathrm{d}x\,\mathrm{d}y \\ \int_S x\tilde{W}(x, y, t)\,\mathrm{d}x\,\mathrm{d}y \\ \int_S y\tilde{W}(x, y, t)\,\mathrm{d}x\,\mathrm{d}y \end{bmatrix} \tag{7}$$

From here, it follows that the values for the piston and the X/Y-tilt terms depend on the aperture size and geometry. This dependence is known as the aperture effect [8,12–14]. For symmetric apertures, like circular or rectangular ones, with the center of the aperture at $x = 0, z = 0$, all off-diagonal terms in Eq. (7) are zero; and the expressions for the unsteady piston and X/Y-tilt terms become

$$C(t) = \frac{\int_S \tilde{W}(x, y, t)\,\mathrm{d}x\,\mathrm{d}y}{\int_S \mathrm{d}x\,\mathrm{d}y}, \qquad A(t) = \frac{\int_S x\tilde{W}(x, y, t)\,\mathrm{d}x\,\mathrm{d}y}{\int_S x^2\,\mathrm{d}x\,\mathrm{d}y},$$
$$B(t) = \frac{\int_S y\tilde{W}(x, y, t)\,\mathrm{d}x\,\mathrm{d}y}{\int_S z^2\,\mathrm{d}x\,\mathrm{d}y} \tag{8}$$

As mentioned before, the X/Y-tilt components, $A(t)$ and $B(t)$, are almost always corrupted by mechanical distortions and are typically removed from the experimental data. Also, for traditional Shack–Hartmann wave-front sensors, the piston mode $C(t)$ cannot be sensed; as a consequence, it is also removed from the measured wave fronts. Thus, only the higher-order component $W(x, y, t)$ can be properly measured. The question becomes the following: Is it possible to recover the aero-optical X/Y tilt and the piston components, as well as to reconstruct the apertured wave fronts $\tilde{W}(x, y, t)$ if only the higher-order wave fronts $W(x, y, t)$ are available? It will be demonstrated that under a few fairly generic assumptions, it is possible. Additionally, the necessary guidelines and requirements to do so will be outlined.

II. Stitching Method

As discussed earlier in this paper, the X/Y-tilt and piston components are typically removed from experimental wave-front data due to corruption from mechanical vibration of the various components of the experimental setup. Vibrations of the optical elements, optical table, wind tunnel, aircraft, etc., also manifest as unsteady X/Y-tilt and piston modes in the wave-front data [8,15]. As demonstrated in Eq. (8), these modes depend on the aperture size and geometry. As these modes are typically removed from the true wave fronts, the statistics of the resultant measured wave fronts $W(x, y, t)$ will also depend on the aperture size. The aperture dependence of these statistics is referenced in the literature as the aperture effects. This dependence has been extensively studied by other researchers [8,14,16,17]. In this work, we propose a method for correcting experimentally measured wave-front data for aperture effects and, in the process, recover the aero-optical component of the jitter.

The method proposed in this work is denoted as the "stitching method," and it necessitates making two assumptions in order to implement it. First, the flow must be primarily convective; that is, the wave fronts can be described as $\tilde{W}_{\text{true}}(x - U_c t, y)$. In other words, the flow must satisfy Taylor's frozen flow hypothesis [18]. Second, the true wave front must be continuous in both space and time. The convective and continuity requirements prevent the stitching method from being used to analyze flows that contain stationary or nonconvective features, such as unsteady shocks at transonic and supersonic speeds [19] or branch points brought about through deep turbulence [20–22].

A. Stitching Concept

In the following, we will outline a generic approach to extract unsteady piston $C(t)$ and X/Y-tilt terms, $A(t)$ and $B(t)$, and ultimately recover the true wave front $\tilde{W}_{\text{true}}(x, y, t)$ or, if needed, the apertured wave front $\tilde{W}(x, y, t)$. This approach assumes only the high-order (i.e., piston/X/Y tilt removed) wave fronts $W(x, y, t)$ are known and the flow satisfies the two aforementioned requirements.

Let us consider a purely convective true wave front traveling along the x direction with a constant convective speed of U_c, $\tilde{W}_{\text{true}}(x, y, t) = \tilde{W}_{\text{true}}(x - U_c t, y)$. At a given time instant t_1, the true wave front is schematically shown as a thin black line in Fig. 2a. To simplify the illustration of the stitching method, we will plot only one-dimensional (1-D) wave fronts. For a given aperture, identified as two vertical dashed lines in Fig. 2a, the wave front at this time instant over the aperture is defined as $\tilde{W}_1(x, y) \equiv \tilde{W}_{\text{true}}(x - U_c t_1, y), (x, y) \in S$; and it is indicated as a thick black line in Fig. 2a. Using Eq. (3), the apertured wave front can be represented as a sum of the piston and X/Y-tilt components, as well as the higher-order wave front,

$$\tilde{W}_1(x, y) = C_1 + A_1 x + B_1 y + W_1(x, y) \tag{9}$$

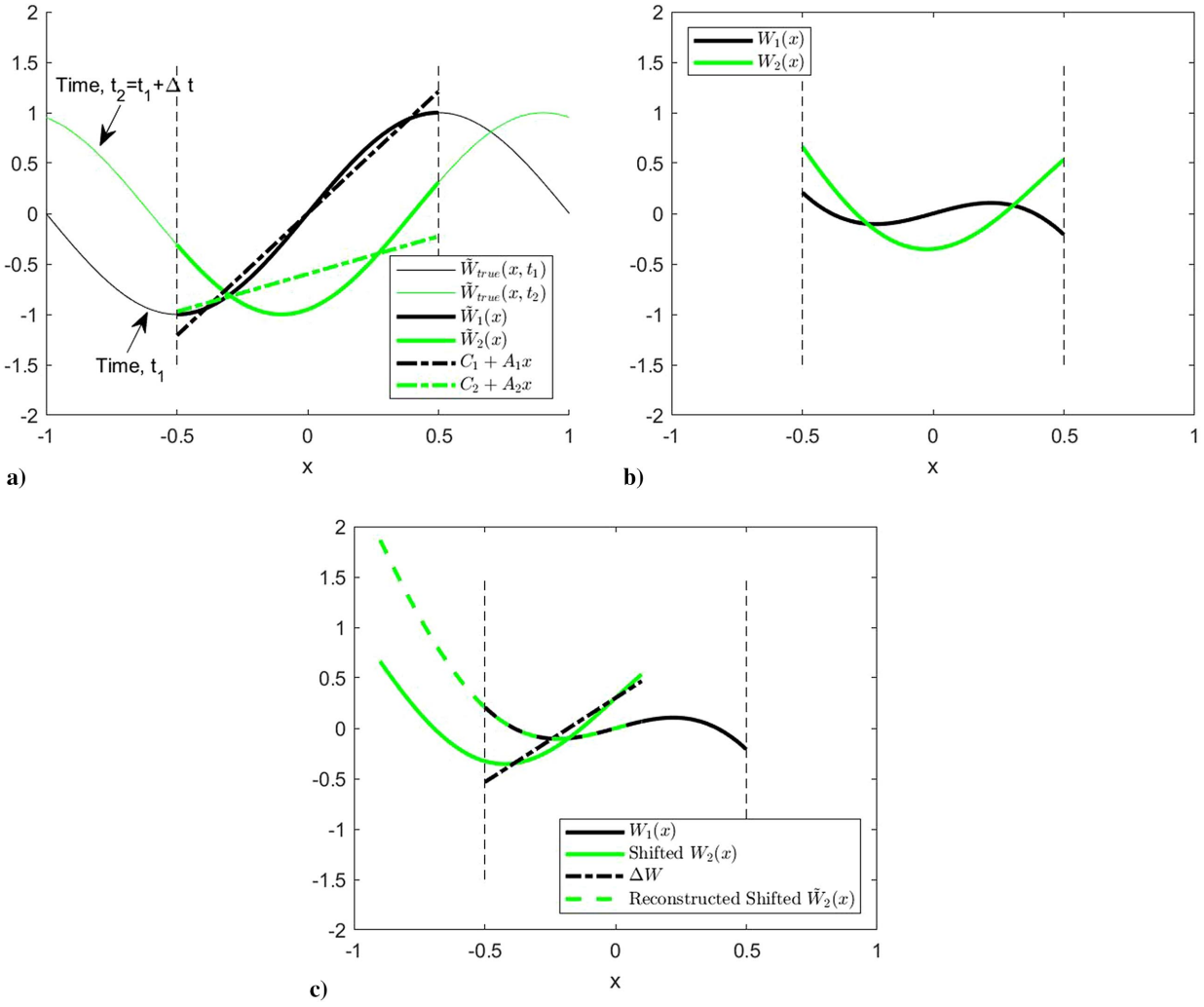

Fig. 2 Representations of a) true convective wave front $\tilde{W}_{\text{true}}(x,t)$ at two different times (thin lines), apertured wave fronts (thick lines), and their piston/tilt components inside aperture (dashed–dotted lines); b) piston/tilt-removed wave fronts; and c) $W_1(x)$ (black line), shifted $W_2(x-\Delta x)$ (green line), difference ΔW (dashed–dotted line), and reconstructed shifted $\tilde{W}_2(x-\Delta x)$ (dashed line).

where A_1, B_1, and C_1 terms can be computed using Eq. (8). The piston and the tilt term $C_1 + A_1x$ is plotted as a dashed–dotted black line in Fig. 2a.

At another time instant, $t_2 = t_1 + \Delta t$, the wave front convects over the aperture by the distance of $\Delta x = U_c\Delta t$ and is plotted as a thin green line in Fig. 2a. Therefore, it has a different apertured wave front over the fixed aperture, $\tilde{W}_2(x,y) \equiv \tilde{W}(x - U_c(t_1 + \Delta t), y)$, shown as a thick green line in Fig. 2a. Similar to $\tilde{W}_1$, $\tilde{W}_2$ inside the aperture can also be split into the piston, X/Y-tilt, and higher-order terms:

$$\tilde{W}_2(x,y) = C_2 + A_2x + B_2y + W_2(x,y) \tag{10}$$

Because $\tilde{W}_2$ is spatially different from $\tilde{W}_1$, the terms C_2, A_2, and B_2 are different from C_1, A_1, and B_1. It can be seen in Fig. 2a, where both piston/tilt components $C_1 + A_1x$ and $C_2 + A_2x$ are plotted as dashed–dotted black and green lines, respectively. In practice, only piston/tilt-removed $W_1(x,y)$ and $W_2(x,y)$ over the aperture are known and shown in Fig. 2b.

On the other hand, since the wave front is purely convective, the apertured $\tilde{W}_2$ over the fixed aperture is simply a spatially shifted version of $\tilde{W}_1$

$$\begin{aligned}\tilde{W}_2(x,y) &\equiv \tilde{W}_{\text{true}}(x - U_c(t_1 + \Delta t), y) = \tilde{W}_{\text{true}}(x - U_c\Delta t - U_ct_1, y)\\ &\equiv \tilde{W}_1(x - \Delta x, y)\end{aligned} \tag{11}$$

Thus, $\tilde{W}_2$ provides information about the true wave front in the region, shifted upstream of the aperture by Δx. Thus, the wave fronts, collected over the aperture at later times, can be used to reconstruct the true wave front farther upstream of the aperture.

When the measured W_2 is shifted by Δx, it does not coincide with the measured W_1 in the overlapping region, as shown in Fig. 2c. This is expected because the different piston/tilt components were removed from the corresponding apertured wave fronts. It also means that the difference between W_1 and the shifted W_2 inside the overlapping region should only be a linear function in space, shown as a dashed–dotted line in Fig. 2c:

$$\begin{aligned}\Delta W(x \in \text{Overlap}, y) &= W_2(x - \Delta x, y) - W_1(x,y)\\ &= (D_1 + D_2x + D_3y)_{\text{Overlap}}\end{aligned} \tag{12}$$

All the D terms in Eq. [12] can be directly computed by fitting a spatial plane to the difference.

Note that for a fixed aperture of size Ap in the x direction (that is, $x \in [-Ap/2, Ap/2]$), the difference in Eq. (12) is defined only inside the overlapping region for spatial points $x \in [-Ap/2, Ap/2 - \Delta x]$, with the spatial extent of $L_{\text{Overlap}} = Ap - \Delta x$ in the x direction; see Fig. 2c. Obviously, if $\Delta x = U_c\Delta t > Ap$, there is no overlapping region to compute the difference. Therefore, the sampling frequency of the wave-front collection, $f_s = 1/\Delta t$, should be larger than the U_c/Ap. In practice, as will be shown later, the overlap region should

be about 50% of Ap or larger, giving an even higher required sampling frequency.

Finally, due to the requirement that wave fronts be continuous, the wave fronts should be the same in the overlapping region. To guarantee it, the linear difference, computed using Eq. (12), can be added to the shifted W_2 to reconstruct the true wave front upstream of the aperture:

$$\text{Reconstructed shifted } \tilde{W}_2(x-\Delta x, y) = W_1(x,y) + (D_1 + D_2 x + D_3 y)_{\text{Overlap}} \quad (13)$$

The reconstructed shifted $\tilde{W}_2$ is shown in Fig. 2c as a thick dotted line. In construction, both W_1 and the reconstructed shifted $\tilde{W}_2$ exactly match in the overlapping region.

If the third measured wave front, $\tilde{W}_3(x,y) \equiv \tilde{W}_{\text{true}}(x - U_c(t_1 + 2\Delta t), y)$, measured at the latter time of $t_1 + 2\Delta t$, is given, the outlined procedure is applied to the reconstructed shifted $\tilde{W}_2$ and the W_3, shifted upstream by $2\Delta x$, to recover a linear correction function. Once the linear correction function is computed, it is added to the shifted W_3 to restore the wave-front continuity.

The entire process can be repeated for each wave front given in the time sequence. At every step, another properly shifted and linearly corrected wave front is added to the previously matched or stitched wave fronts, resulting in a continuous wave-front strip, which is recovered upstream of and over the aperture, as shown as a thick line in Fig. 3.

At the end of the procedure, the overall stitched wave front might have a nonzero global X/Y tilt and piston, as seen in Fig. 3. This is because the tilt-removed $W_1(x,y)$ was used as an anchor to start the stitching method, with the unknown amount of piston and X/Y tilt removed from it. By design of the stitching method, it recovers only a differential piston and X/Y tilt between the adjacent wave fronts in order to recover the wave-front continuity. Thus, the unknown X/Y tilt, removed from the first wave front, was essentially removed from all reconstructed wave fronts, resulting in a global nonzero X/Y tilt in the reconstructed wave front. Because it is reasonable to assume that the overall global X/Y tilt in the reconstructed wave front is zero for a sufficiently large reconstructed wave-front strip, we can simply remove the global piston and X/Y tilt from the final reconstructed wave front, as shown in Fig. 3. A detailed discussion and the analyses of the uncertainty associated with this global X/Y-tilt removal can be found in Ref. [23].

B. Computing Convective Speed

As alluded to in the preceding text, the convective velocity of the optical structures is a necessary parameter in order to use the stitching method. More precisely, the common overlapping region between frames is a required quantity; and it must be identified for the stitching algorithm to be applied. The convective velocity of the flow in conjunction with the sampling frequency used in the experiment defines the overlap present in adjacent wave-front images. For certain flows such as boundary layers [14,24,25] and shear layers [26,27], the convective velocity has been extensively studied and can be assumed to be constant and known. More analyses on the assumption of a constant convective velocity in the stitching method can be found in Ref. [23]. If the convective velocity is unknown or believed to be nonconstant but slowly varying in time, a quasi-instantaneous convective velocity can be computed by cross correlating wave fronts with different streamwise offsets. Finding the streamwise shift that corresponds to the largest correlation will give the approximate distance traveled by the optical structures between the two frames. The computed distance traveled by the optical structures can then be divided by the time difference between frames to give the average convective velocity of the optical structures for a given subsequent pair of wave fronts.

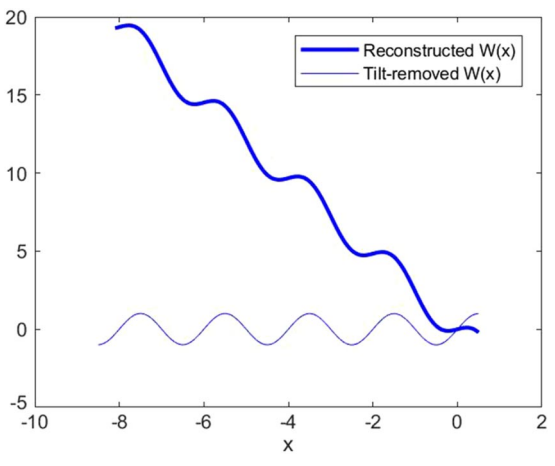

Fig. 3 The final reconstructed wave front plotted with the tilt-removed version.

Recall that from Eq. (12), if W_2 is shifted by $\Delta x = U_c \Delta t$, the difference between the shifted W_2 and W_1 is a linear function only, if the wave front is purely convective. It can be rewritten in the following way:

$$U(D_1, D_2, D_3, \Delta x) = \int_{\text{Overlap}} \{W_2(x-\Delta x, y) - W_1(x,y) - [D_1 + D_2 x + D_3 y]\}^2 \, dx\, dy \quad (14)$$

where the overlap region depends on the shift Δx. The U function is positive and, for purely convective wave fronts, has a minimum of zero if $\Delta x = U_c \Delta t$. For any other streamwise shifts, the U function will be positive. Thus, Eq. (14) can be used to compute both D coefficients and the spatial shift Δx by finding the minimum value of U. Because U is a linear function of D coefficients, for a given guess of the shift, D coefficients can be found in a similar fashion as in deriving Eq. (7). After substituting D coefficients into Eq. (14), the values of U can be found for different guesses of the spatial shift. The minimum of U will give the proper value of the spatial shift, which is needed to apply the stitching method. It can also be used to calculate the quasi-instantaneous convective speed, corresponding to the pair of the wave fronts.

As will be shown later, if the aperture is sufficiently large, the instantaneous X/Y tilt (removed from each frame) is small, and the measured wave fronts are close to the true wave fronts. In this case, we can use the standard cross-correlation function to find Δx:

$$\text{Corr}(\Delta x) = \int_{\text{Overlap}} W_2(x-\Delta x, y) W_1(x,y) \, dx\, dy \quad (15)$$

For pure convective wave fronts, the correlation is maximum if $\Delta x = U_c \Delta t$. Because the wave fronts are given over discrete spatial points, the standard parabolic fit near the maximum can be used to improve the estimate of Δx.

Figure 4 shows an example of computing the spatial shift using two realistic two-dimensional wave fronts measured over a rectangular aperture. The two wave fronts have the same structure, outlined by a dotted line, located at different spatial regions for each wave front. If the wave front W_2 is shifted properly, the outlined structure in the shifted wave front will match the structure in W_1 in the overlapping region, resulting in the largest correlation value.

C. Average the Adjacent Frames

In practice, the structure in the overlapping region might not be exactly the same for the adjacent wave fronts. One source of the mismatch is that the structure might slightly evolve between the times the two wave fronts were collected. Another source is measurement noise. To avoid spatial discontinuity in the reconstructed wave front on the perimeter of the overlapping region, a linear weighting approach was used where, in the overlapping region between the two wave fronts, each wave front is multiplied by a weighting function that varies linearly in the streamwise direction from zero

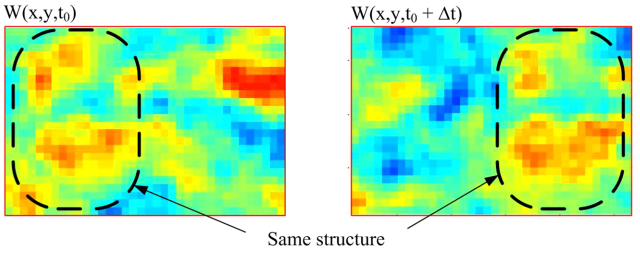

a) The two frames to be stitched have common structures

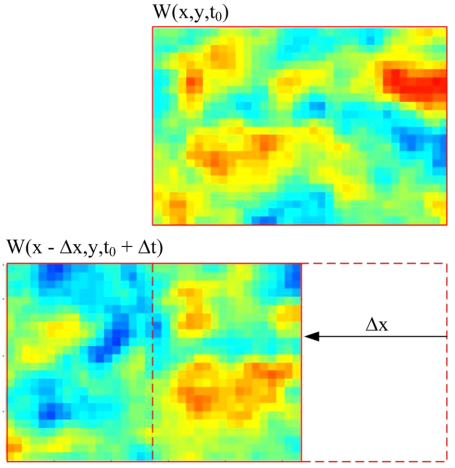

b) The frame represented as, $W(x, y, t + \Delta t)$ is shifted in space

Fig. 4 Demonstration of the computation of spatial shift (overlap). The quantity Δx can be found using a cross correlation between the wave fronts using Eq. (15). Flow direction is from left to right.

to one, as demonstrated in Fig. 5. The reconstructed wave front in the overlapping region is a sum of the adjacent weighed wave fronts.

In summary, the stitching method is executed in a loop. At each iteration of the loop, the following steps are performed:

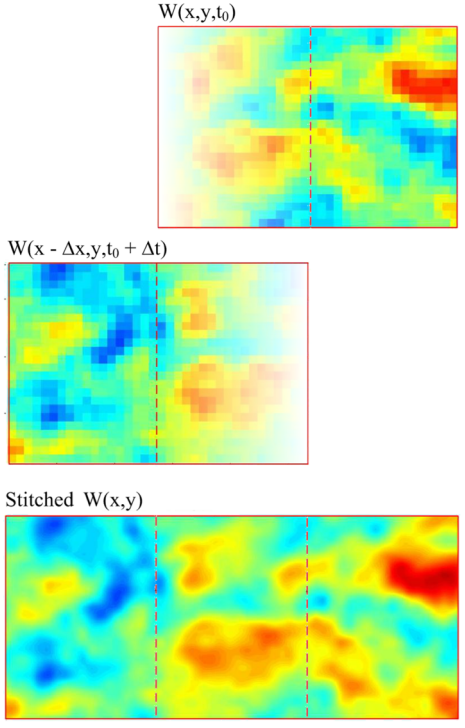

Fig. 5 Illustration of final averaging step in stitching algorithm. A spatially linear weighting function is applied to each wave front in overlapping region, and the resulting reconstructed stitched wave front is taken to be a sum of two adjacent weighed wave fronts.

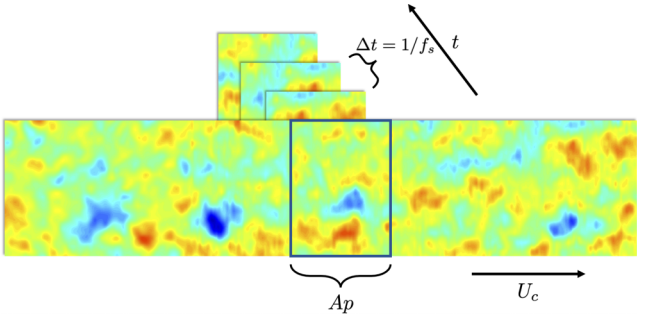

Fig. 6 Variable aperture approach applied to a stitched wave front.

1) Compute the spatial offset Δx between two adjacent wave fronts using either Eq. (14) or, for large apertures, Eq. (15).

2) Compute the linear correction function by performing a linear fit to the difference between the properly shifted wave fronts using Eq. (12).

3) Compute the reconstructed shifted wave front using Eq. (13).

4) Compute the spatially extended wave front by averaging over the properly weighed wave fronts, as illustrated in Fig. 5.

D. Variable Aperture Approach

Once the wave fronts have been stitched by adding the proper amount of the aero-optical piston and X/Y tilt to each shifted wave front to ensure the continuity of the resulted wave front, we can then begin the process of recovering the aero-optical component of the jitter. As stated earlier in this paper, the stitching method produces long strips of wave-front data, $\hat{W}^{\text{stitch}}(x - U_c t, y)$, where the reconstructed wave front is convected at a constant speed U_c. Again, it is important to note that these new time series of wave-front data have been corrected for any corruptions caused by mechanical vibration present in the experiment. From the recovered wave front, both the local jitter or local deflection angles and the global tilt for a given aperture can be recovered. To recover the local deflection angle, we can use the definition of the deflection angle as a negative gradient of the wave front. For instance, the true streamwise deflection angle, denoted as $\tilde{\theta}$, can be computed as

$$\tilde{\theta}(x, y, t) = -\frac{d\tilde{W}^{\text{stitch}}(x - U_c t, y)}{dx}$$

Similarly, the global aero-optical jitter can be recovered by applying Eq. (7) or, for round or rectangular apertures, by using Eq. (8). Since we now have long strips of the reconstructed wave front, we can re-aperture them to any arbitrary aperture size or to match the experimental aperture. To do so, the long stitched wave front is "pulled" through the aperture of arbitrary size Ap at a velocity of U_c. Snapshots are then taken at a sample rate of f_s to build back up a stack of reconstructed wave fronts. This process can be seen schematically in Fig. 6.

Now that the times series of wave-front data with arbitrary aperture size is generated and the global aero-optical tilt is extracted from each wave front, we can study the global tilt statistics for different apertures. In the following sections, we will develop a model for the aero-optical global tilt and apply the stitching technique to investigate the statistics of aero-optical global tilt created by a forced shear layer.

III. One-Dimensional Model of the Global Tilt

The main quantity of interest in this work is the aero-optical component of the global tilt in the streamwise direction, X tilt, present in experimental wave-front data. This quantity was denoted as the A coefficient in the previous sections to simplify the derivation of the stitching method, but we now would like to use θ_G notation for the rest of the paper to explicitly emphasize a connection to a local jitter θ. In this paper, we will focus only on the streamwise component of the global jitter, and we will not consider the spanwise global Y tilt. We have shown that the stitching method is one option in recovering the

global tilt. In this section, we will present a one-dimensional filter model that can be used to predict the amplitude of the global streamwise X tilt in case of a purely convective single-harmonic wave front. For simplicity, for the rest of the paper, we will refer to it as the global tilt.

The foundation for the filter model presented in this section was first developed in Ref. [8]. The transfer function G_A, defined later in the section and used in the filter model, was initially derived in Ref. [13]. In this work, we will first rederive the filter model for completeness and then apply it in a new way as a means to predict the aero-optical component of the global tilt from local deflection angle spectra.

We begin with a one-dimensional purely convecting true wave front consisting of a single harmonic:

$$\tilde{W}_{\text{true}}(x,t) = \sin\left[\frac{2\pi}{\Lambda}(x - U_c t)\right] \tag{16}$$

where U_c is the convective velocity of the wave front, and Λ is the spatial period of the wave front. Ultimately, we are interested in how the global tilt changes with the aperture size Ap. To do this, we consider the definition of global tilt, which is defined in Eq. (7).

To get an explicit equation for the streamwise global tilt $\theta_G(t; Ap)$, we can substitute the model wave front given in Eq. (16) into Eq. (8) to obtain

$$\begin{aligned}\theta_G(t) &= \frac{6\Lambda\left[\Lambda\sin\left(\frac{\pi Ap}{\Lambda}\right) - \pi Ap\cos\left(\frac{\pi Ap}{\Lambda}\right)\right]\cos\left(\frac{2\pi t U_c}{\Lambda}\right)}{\pi^2 Ap^3} \\ &= k_x\cos(2\pi f t)\cdot\left[3\frac{\sin(\pi Z) - (\pi Z)\cos(\pi Z)}{(\pi Z)^3}\right]\end{aligned} \tag{17}$$

where $f = U_c/\Lambda$ is the frequency, which is associated with the traveling wave front, $Z \equiv Ap/\Lambda = (Apf)/U_c$, and $k_x = 2\pi/\Lambda$ is the structure wave number. Recall that the local streamwise jitter is a negative spatial derivative of the true wave front, $\theta = -d\tilde{W}_{\text{true}}/dx$. Thus, for the model wave front, the local streamwise jitter at the center of the aperture, $x = 0$, is $\theta(t) = k_x\cos(2\pi f t)$. By comparing this expression with Eq. (17), we recognize that the first term of Eq. (17) is simply the local jitter. Therefore, the term in square brackets in Eq. (17) acts as a transfer function from local jitter θ to global tilt θ_G. We denote this transfer function as G_A:

$$G_A(Z) = 3\frac{\sin(\pi Z) - (\pi Z)\cdot\cos(\pi Z)}{(\pi Z)^3} \tag{18}$$

A plot of $G_A(Z)$ is presented in Fig. 7.

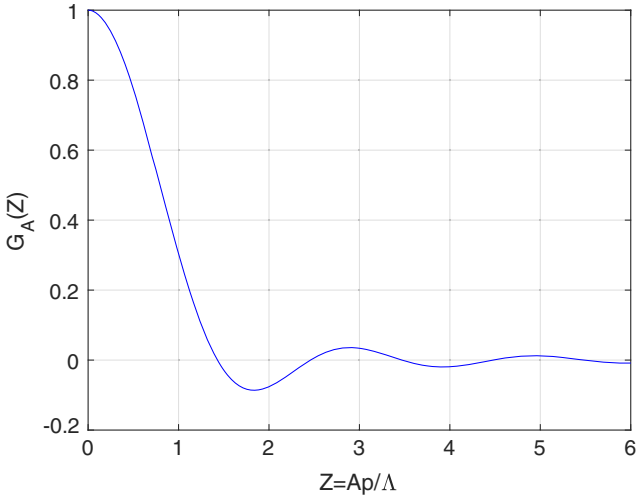

Fig. 7 Global tilt transfer function $G_A(Z)$

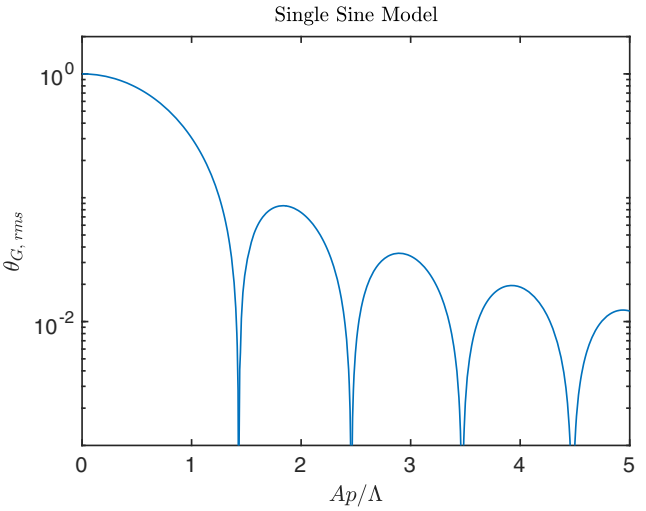

Fig. 8 Normalized rms of global tilt $\theta_{G,\text{rms}}$ vs $Z = Ap/\Lambda$ for the single sine model

For a single frequency traveling harmonic, $G_A(Z)$ relates the amplitude of local jitter to the amplitude of global tilt over a given aperture, $\theta_G(t; Z) = G_A(Z)\theta(t)$. As a consequence, the autocorrelation spectral densities for local jitter and global tilt are related as well:

$$S_G(f; Z) = (G_A(Z))^2 S_\theta(f) \tag{19}$$

where the transfer function acts as a low-pass filter. Thus, by measuring only the autocorrelation spectral density of the local jitter (deflection angle) $S_\theta(f)$ and assuming a purely convective wave front, we can compute the autocorrelation spectral densities of the global tilt and determine the global tilt rms value $\theta_{G,\text{rms}}$ for different apertures:

$$\theta_{G,\text{rms}}(Ap) = \left[\int_{-\infty}^{\infty} S_\theta(f)\cdot G_A(Z)^2\,\mathrm{d}f\right]^{1/2} \tag{20}$$

where, again, $Z = Apf/U_c$. This is a crucial result, and it is worth restating. By measuring the *local* jitter only, we can approximate the global tilt for *any aperture* as long as the spatial growth is small enough, the wave fronts can be treated as purely convective, and an uncorrupted local jitter measurement can be obtained. Because local jitter is a point quantity, and therefore is not influenced by aperture effects, this is an impactful result. Remember, the local jitter still can be corrupted by mechanical vibrations, and the stitching method can be used to remove these contamination, as discussed in the previous section.

It is easy to see from Eq. (20) that if a wave front is approximated as a sine wave, as in Eq. (16), the rms value of global tilt $\theta_{G,\text{rms}}$ reduces to

$$\theta_{G,\text{rms}}(Z) = \theta_{\text{rms}}\cdot|G_A(Z)| \tag{21}$$

The rms of global tilt from Eq. (21), plotted for various aperture sizes, is shown in Fig. 8 where, for convenience, the value of the local jitter θ_{rms} was set to be unity.

The global tilt becomes smaller for larger apertures. Also, the sharp dropouts present in $\theta_{G,\text{rms}}$ are related to Z values, where $G_A(Z) = 0$. From Eq. (18), these Z values satisfy the equation $\tan(\pi Z) = \pi Z$ with solutions $Z = 1.43, 2.46, 3.47, 4.48, \ldots$. At these Z values, the global tilt is exactly zero for any amplitude of the local jitter in the case of a single-harmonic wave front.

IV. Uncertainty Analysis

In the application of the stitching method, several factors are important. In this section, we will present a parametric study on the impact of aperture size, spatial resolution, temporal resolution, and noise on the accuracy of the stitching method. Just as in Sec. III, we will use a single sine wave with a known convective velocity, given in Eq. (16), to perform the uncertainty analysis. In our analysis, we

assume that the convective speed is constant. Although a slowly varying convective speed will undoubtedly add additional uncertainty to the reconstruction of the global tilt, this effect is not addressed here and is left for the future work. As a starting point, a long time series of wave fronts over a fixed aperture with given discrete spatial points was generated. At every frame in time, the global tilt and piston were computed using Eq. (8) and saved as a time series. To simulate the experiments, the global tilt and piston were removed from each frame to form a time sequence of the higher-order wave fronts. The time series of global tilt was then used to compute the root mean square of the tilt $\theta_{G,\mathrm{rms}}$. This parameter will be used to evaluate the accuracy of the stitching method.

To further model the experimental conditions, once the tilt and piston were removed from all wave fronts, zero-mean one-dimensional Gaussian noise with a standard deviation ϵ was added to each time-frame. In practice, the noise is sensor related; for a Shack–Hartmann wave-front sensor, it mostly comes from uncertainty in computing local deflection angles used to reconstruct wave fronts. Additional uncertainly is also sourced from the least-squares fit of the wave front to the measured slopes. In addition, note that the sine wave in Eq. (8) has a fixed amplitude of unity. In general, ϵ should be viewed as a percentage of noise relative to the wave-front amplitude. The resultant wave-front sequence was input into the stitching method. The stitching method uses each frame to reconstruct one long wave-front strip in space. If the wave-front stitching algorithm did a perfect job of reconstruction, there would be no difference between the stitched wave front and the original sine wave. It was already shown in Sec. III that with no noise added, and with a sufficient amount of wave-front frames to stitch, the stitching method converges onto the original sine wave. The varying value of noise added to each wave-front frame changes the computed tilt and piston in the overlapping region. This deviation from the actual tilt and piston is the major source of uncertainty.

Once the stitched wave front has been determined, the stitched wave front was apertured down just as was previously done with the original sine wave. On this new wave-front time series, the reconstructed global tilt was computed for each frame. The temporal rms of the global tilt for the original sine wave $\theta_{G,\mathrm{rms}}$ and for the wave front produced by the stitching method $\theta^{\mathrm{stitch}}_{G,\mathrm{rms}}$ were then compared. The error between the two quantities is a global tilt error, which was defined as follows:

$$\Sigma\left(\frac{Ap}{\Lambda}, N_p, \mathrm{Overlap}, \epsilon\right) = \frac{|\theta_{G,\mathrm{rms}} - \theta^{\mathrm{stitch}}_{G,\mathrm{rms}}|}{\theta_{G,\mathrm{rms}}} \tag{22}$$

where Ap/Λ is the nondimensional aperture size, and N_p is the number of spatial points contained in the wave front over the aperture. The parameter of Overlap $= (Ap - \Delta x)/Ap$, where $\Delta x = U_c/f_s$, is the percentage of overlap between frames, relative to the aperture size, and is determined by the convective velocity U_c and the sampling frequency f_s. Finally, ϵ is the standard deviation of the one-dimensional Gaussian random noise added to each 1-D wave-front frame in time.

In Fig. 9, the resultant error in global tilt Σ with $\epsilon = 0.01$ is plotted for various overlap percentages. The three curves in each figure represent different numbers of points in each wave front: $N_p = 20, 30, 50$.

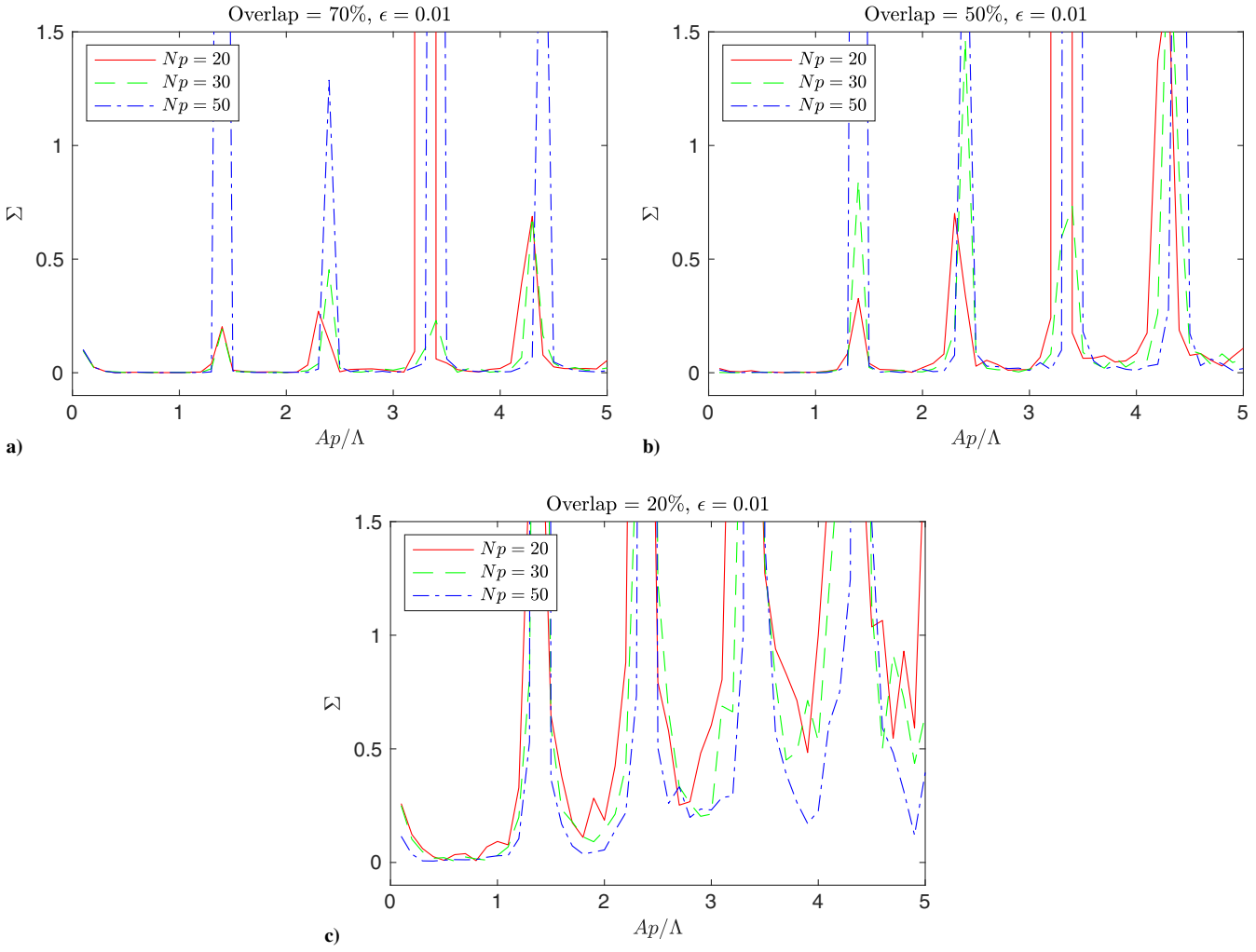

Fig. 9 Error in estimating global tilt Σ defined in Eq. (22) for different number of spatial points N_p for a) $\epsilon = 0.01$, Overlap = 70%; b) $\epsilon = 0.01$, Overlap = 50%; and c) $\epsilon = 0.01$, Overlap = 20%.

For the large parameter of Overlap = 70%, we see that the stitching method does a very good job predicting the global tilt, except for at four points. At those four locations ($Ap/\Lambda \approx 1.4, 2.5, 3.5, 4.5$), the real global tilt for the sine wave approaches zero, as shown in Fig. 8. This causes the resultant error to tend toward infinity. For the following analysis, we will ignore these four locations and focus on the error at other aperture sizes.

For the parameter of Overlap = 50%, the stitching method still does a good job across all aperture sizes, except at the same four locations mentioned before. For the parameter of Overlap = 20%, we begin to see the effects of spatial resolution. Because the number of points N_p is fixed as the aperture grows, the spatial resolution decreases. The simulation was done in this way to mimic the experiment. In typical experiments, the number of points across the aperture is usually fixed by the lenslet array size and magnification of the optical setup. The number of points across the aperture seen in the experiment is typically between 25 and 50. For very poor spatial resolution of $N_p = 20$ at the parameter of Overlap = 20%, the global error is larger than 0.2 for $Ap/\Lambda > 2$, and so the stitching method cannot accurately reproduce the global tilt. But, if a sufficient number of points of $N_P > 50$ is used, even at this low overlap percentage, the stitching method is still within approximately 20% of the actual value of $\theta_{G,\mathrm{rms}}$.

We can now plot the same error but for an increased noise parameter. The various error plots for $\epsilon = 0.05$ can be seen in Fig. 10.

For the large parameter of Overlap = 70%, we see that the stitching method does a good job when for the higher spatial resolution of $N_p > 30$. Ignoring the performance dropouts caused by the real global tilt reaching a minimum, for apertures smaller than $Ap/\Lambda \approx 3$, the stitching method maintains $\Sigma < 0.2$ for all spatial resolutions. The error begins to increase significantly near $Ap/\Lambda \approx 3$ for the $N_p = 20$ and 30 cases.

For the parameter of Overlap = 50%, we once again see the impact of spatial resolution. With the increased noise parameter when compared to the $\epsilon = 0.01$ simulations, the stitching method becomes more sensitive to spatial resolution and overlap percentage. The error begins to increase significantly above $Ap/\Lambda \approx 2$ for the $N_p = 20$ and 30 cases. The $N_p = 50$ case begins to see a significant reduction in performance above $Ap/\Lambda \approx 3$.

For the parameter of Overlap = 20%, we see an overall poor performance across all apertures and spatial resolutions. With this increased level of noise, there is not enough common information in the frames for the stitching method to predict the global tilt.

In summary, the presented uncertainty analysis revealed that having an *Overlap* value of at least 50% would result in a reasonably small error of $\Sigma < 0.1$ in reconstructing the global tilt using the stitching method if the experimental noise, relative to the wavefront amplitude, is less than a few percent. Using the definition of the *Overlap* parameter, it provides a recommendation for choosing the sampling frequency, namely, $f_s > 2U_c/Ap$. The stitching method tends to work better for small or moderate aperture-to-scale ratios: $Ap/\Lambda < 3$.

V. Experimental Setup

The experiments were conducted to develop and provide evidence for the efficacy of the stitching method. All wind-tunnel experiments

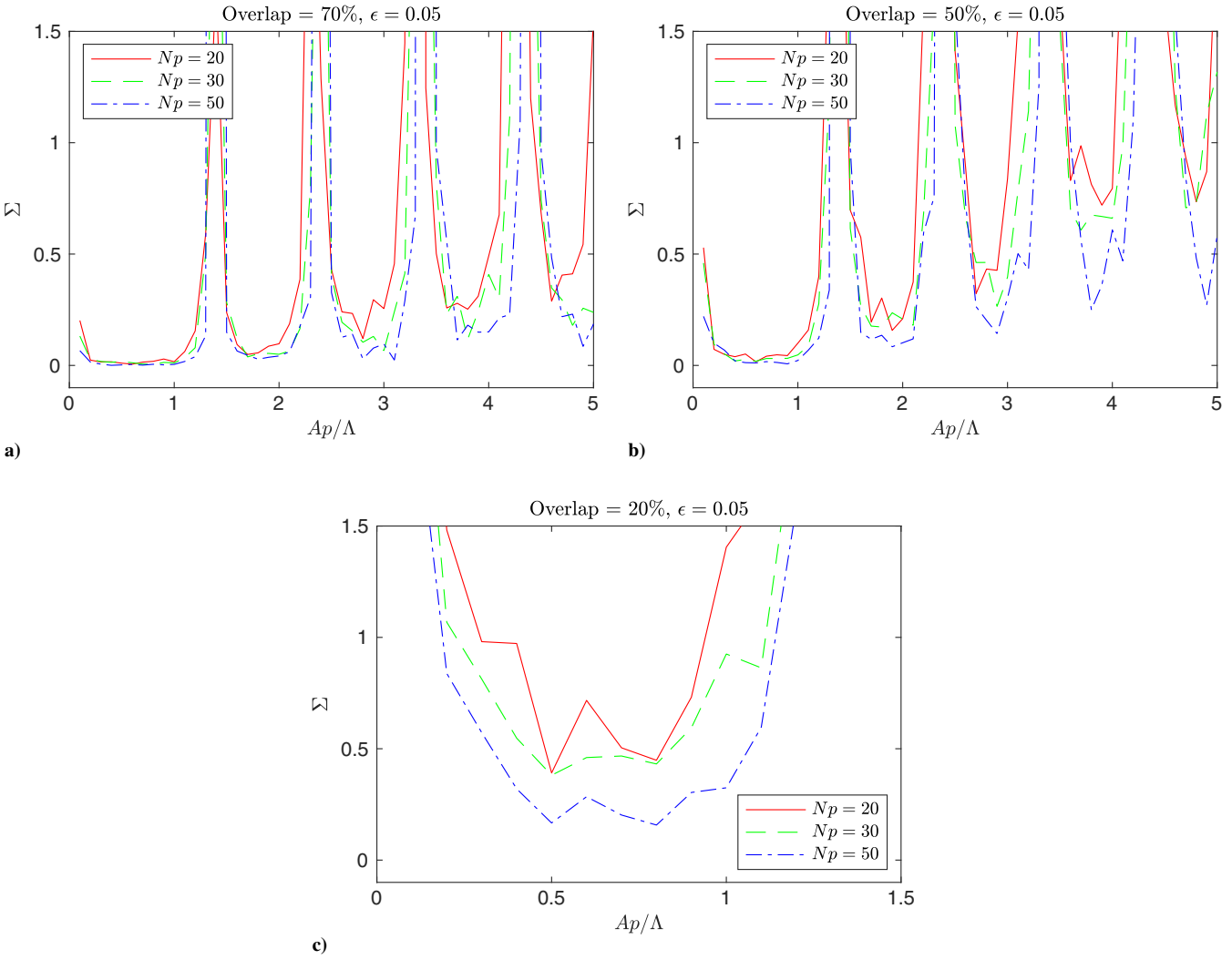

Fig. 10 Representations of the global tilt error, ϵ, for a) $\epsilon = 0.05$, Overlap = 70%, b) $\epsilon = 0.05$, Overlap = 50%; and c) $\epsilon = 0.05$, Overlap = 20%

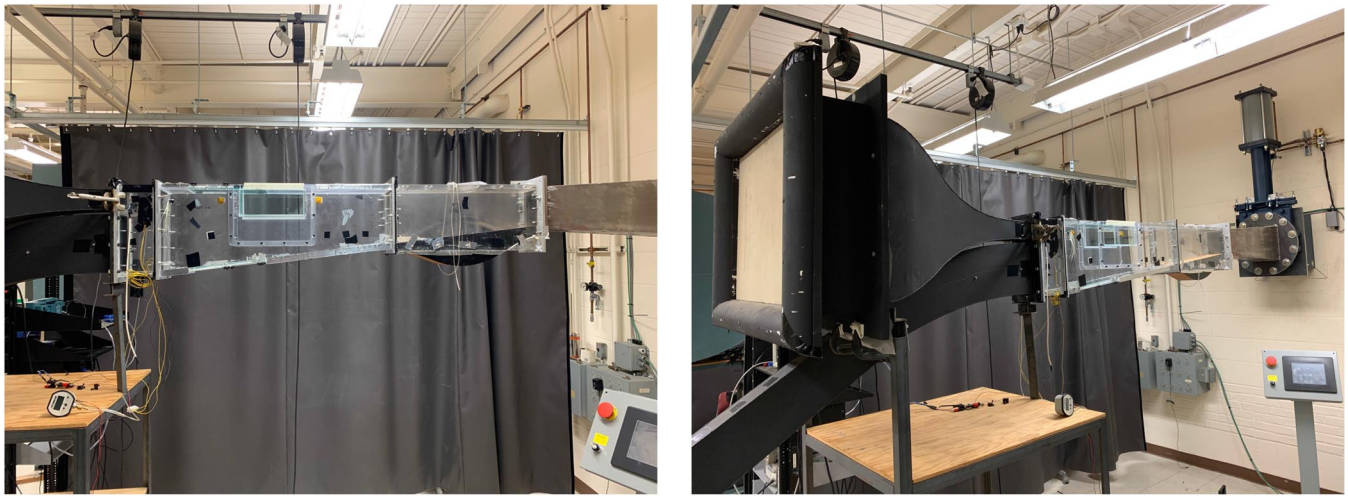

Fig. 11 Shear-layer test section installed in the Tri-Sonic Wind Tunnel Facility.

were conducted at the University of Notre Dame's Tri-Sonic Wind Tunnel Facility. The facility is an indraft tunnel design with interchangeable test sections. Photographs of the shear-layer test section can be seen in Fig. 11.

As shown in Fig. 11, the test section has two inlets. The upper inlet is the high-speed inlet, and the lower inlet is for low-speed flow. The high-speed inlet is square and has a 48.5-to-1 contraction nozzle that reduces the area from 0.4227 to 0.0087 m^2. The low-speed section undergoes a slight expansion from 0.0157 to 0.0276 m^2. The low-speed inlet is filled with narrow tubes that dropped the total pressure of the low-speed flow due to their wall shear stress. The velocity ratio of the shear layer could be adjusted by adjusting the overall length of the low-speed inlet. The two flows are separated by a splitter plate 76.2 mm from the upper wall, shown in Fig. 12a. The test section is 101.6 mm in width. The high-speed inlet was set to $M = 0.6$, whereas the low-speed section was set to $M = 0.1$. The static pressure was matched at the splitter plate. The lower wall of the test section is sloped at 6.35 deg to compensate for the viscous-related total pressure losses and to ensure the static pressure in the test section is constant in the streamwise direction. Additional details about Tri-Sonic Wind Tunnel Facility can be found in Ref. [28].

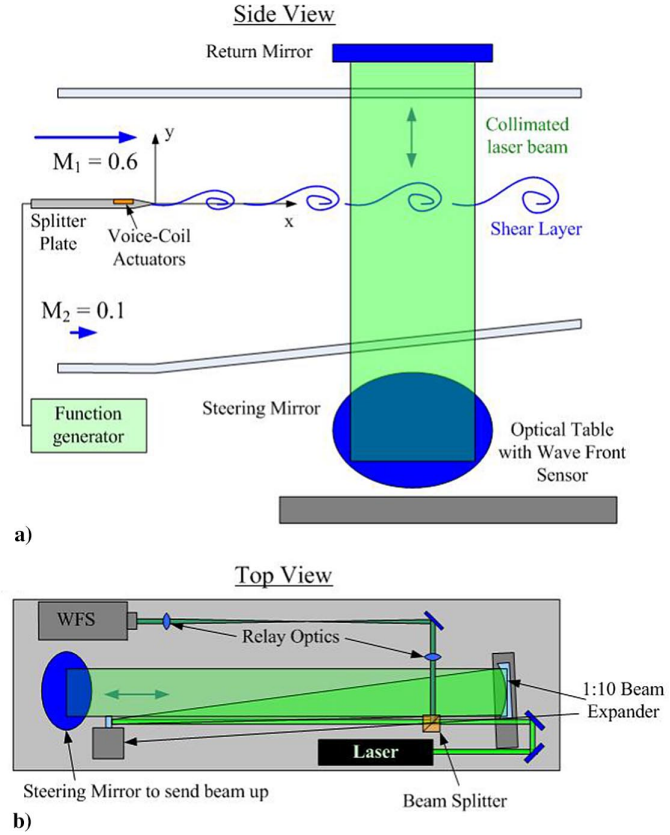

Fig. 12 Schematic of Notre Dame's Tri-Sonic Facility with the shear-layer test section installed: a) side view of the test section, and b) top view of the optical setup.

A. Shear-Layer Forcing

A regularized shear layer represents a natural candidate for the application of the stitching method due to a presence of well-defined vortical structures and the related aero-optical distortions. To regularize shear layer, external forcing was used. An in-depth analysis on the forcing technique can be found in Refs. [28,29], and so only essential information relevant to the current experiment will be provided here. Three voice-coil actuators were mounted on the splitter plate to periodically force the shear layer at the end of the splitter plate. A photograph of the voice-coil actuators mounted to the splitter plate can be seen in Fig. 13a. The voice-coil actuators were Panasonic EAS3P127A 8 Ω, 0.5 W speakers. The speakers were trimmed by about one-fifth of their diameter, as shown in Fig. 13, such that they could be mounted flush to the trailing edge of the splitter plate.

In Ref. [28], it was shown that a forcing signal comprising the fundamental harmonic at the forcing frequency and a 10%-amplitude subharmonic at half of the forcing frequency did the best job at regularizing the shear layer. The forcing frequency for this experiment was chosen to be 640 Hz because it has been shown to be a good choice of forcing frequency to regularize the shear layer for the streamwise location of our measurements [28]. It was found that at this frequency, the edges of the actuators were displaced by about 1 mm from peak to peak [28]. Finally, it was shown in Ref. [28] that the growth rate of the forced shear layer is suppressed over the region of the optical measurements. As the stitching method relies on the assumption of the streamwise homogeneous flow, it makes the forced shear layer a good candidate to apply the stitching method.

B. Optical Measurements

Side and top views of the optical setup used in this work can be seen in Fig. 12. The laser for this experiment was shone in the wall-normal direction (from bottom to top). This can be seen schematically in Fig. 12a. A schematic of the optical setup used is presented in Fig. 12b. For this work, a Neodymium-doped Yttrium aluminium Garnet (Nd:YaG) laser was first expanded to 18 mm using a Melles–Griot refractive beam expander and then passed through a cube beam splitter cube. From the beam splitter, the beam was expanded again to 180 mm using a custom-made off-axis 1 : 10 reflective beam

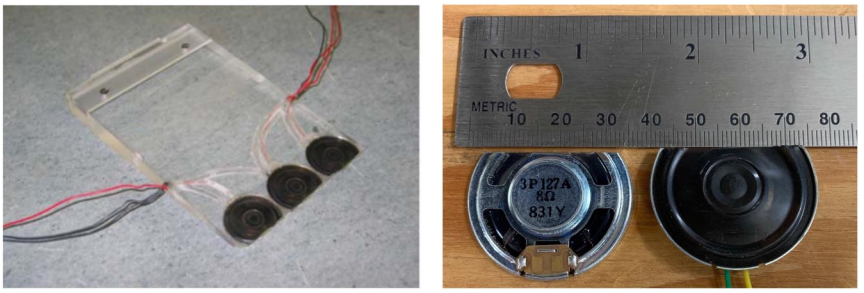

a) b)

Fig. 13 Photograph of a) the voice-coil actuators mounted on the splitter plate, from Ref. [29]; and b) details of the voice-coil actuators.

expander. This 180 mm beam was sent up through the test section and reflected back through the same optical path using a large flat return mirror. This is the so-called double path setup that increases the signal-to-noise ratio of wave-front measurements. The center of the aperture was set at 275 mm downstream of the splitter plate. After the beam splitter cube on the reimaging side of the optical setup, an optical relay comprising two 1500 mm lenses was used. Wave-front measurements were performed using a Vision Research Phantom v1611. Mounted to the camera was a lenslet array with a pitch of 0.3 mm and a focal length of 38.2 mm. The sampling frequency was set at 40 kHz, and time-resolved two-dimensional wave fronts were collected. The collected wave fronts had 36 subapertures in the spanwise direction and 60 subapertures in the streamwise direction. A total number of 45,700 frames were collected. To describe aero-optical results, a frame of reference was chosen with the x axis denoting the downstream direction and the z axis aligned in the spanwise direction. The origin of the frame of reference was chosen to be in the center of the aperture. Table 1 summarizes the parameters related to the data collection. Also, f_s denotes the sampling frequency, f_f denotes the forcing frequency, Ap denotes the aperture size in physical space in the streamwise direction, and Ap_z denotes the aperture size in physical space in the spanwise direction.

Forced shear-layer parameters are given in Table 2. In Table 2, the indices "1" and "2" denote flow quantities in the high- and the low-speed regions of the shear layer, respectively. Λ denotes the size of a large coherent shear-layer structure, defined as a distance between the minima of the autocorrelation function in the streamwise direction. The Λ length was measured from a conventional normalized unbiased autocorrelation function of the forced shear-layer wave front:

$$\rho_W(\Delta x, \Delta z) = \frac{\langle W(x,z,t)W(x+\Delta x, z+\Delta z, t)\rangle_{\text{overlap}}}{\langle W(x,z,t)^2\rangle_{\text{overlap}}} \tag{23}$$

where the angle brackets denote averaging over time and space in the overlapping region. The autocorrelation function and a slice of it in the streamwise direction are plotted in Fig. 14. From Fig. 14b, the structure size was estimated to be $\Lambda = 0.140$ m. Finally, the convective speed of the shear-layer structures was computed as $U_c = \Lambda \cdot f_f = 90$ m/s.

To demonstrate the stitching method for different *Overlap* parameters for a fixed aperture size, the wave-front data were downsampled to two different frequencies: $f_s^{\text{down}} = 4$ and 2 kHz. At these downsampled frequencies, *Overlap* parameters were found to be Overlap $= (Ap - U_c/f_s^{\text{down}})/Ap = 87$ and 75%, respectively. Later, we will refer to these wave-front sets as the full aperture set of 83% and the full aperture set of 75%. To investigate the effect of the aperture size on the accuracy of the global tilt reconstruction, the wave fronts for the $f_s^{\text{down}} = 4$ kHz case were also spatially clipped to an aperture with the same spanwise size but one-half of the full aperture in the streamwise direction, centered in the middle of the full aperture. Instantaneous piston and X/Y-tilt modes were also removed from this dataset. Later, we will refer to the wave-front set over the smaller aperture as the small aperture set. For the small aperture set, *Overlap* is 75%. A summary of all cases is provided in Table 3.

Note that the streamwise extent of the small aperture set is only 0.64Λ. As discussed before, the X/Y-tilt-removal results in a modification of the spatial statistics of the residual wave fronts. As a consequence, important information about wave fronts at spatial scales larger than the aperture size is also removed. Furthermore, even correlations for spatial separations smaller than the aperture will be modified [14]: It is illustrated in Fig. 14b, where the slice of the cross-correlation function for the small aperture set is plotted as a dashed line. The cross-correlation function is significantly different from the one calculated from the full aperture set; for instance, the distance between the local minima was only 0.078 m. The stitching method reintroduces the aero-optical-only component of the piston and the X/Y tilt back to the wave fronts collected over a finite aperture. As a result, the stitching method recovers the lost information and can be used to calculate aero-optical statistics of the wave fronts for any aperture, including large ones.

Table 1 Forced shear-layer experiment parameters

Parameter	Value
Subapertures	36×60
Ap, m	0.180
Ap/Λ	1.27
Ap_z, m	0.108
f_s, Hz	40,000
f_f, Hz	640

Table 2 Forced shear-layer flow parameters with estimated uncertainties

Parameter	Value
M_1	0.60 ± 0.01
M_2	0.100 ± 0.003
a_1, m/s	333 ± 10
a_2, m/s	344 ± 5
U_c, m/s	90 ± 3
ρ_1, kg/m^3	0.99 ± 0.01
Λ, m	0.140 ± 0.005

VI. Results

A. Aero-Optical Environment of the Forced Shear Layer

Figure 15 shows two representative wave fronts at random different time instances for the full aperture set from the forced, regularized shear layer. The wave fronts have well-defined structures,

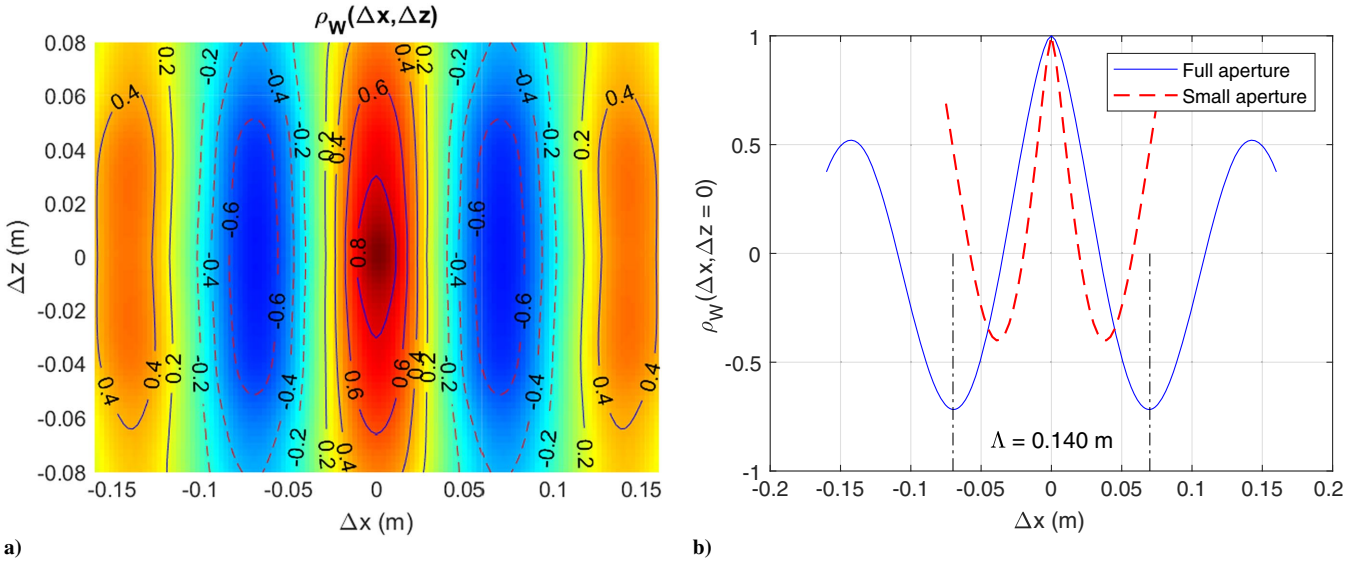

Fig. 14 Representations of a) normalized unbiased autocorrelation of shear-layer wave front, and b) centerline slice of normalized unbiased autocorrelation. Normalized unbiased autocorrelation of small aperture set also plotted as a dashed line.

Table 3 Different apertures and *Overlap* parameters used in the stitching reconstruction

Case	Ap/Λ	f_s^{down}, Hz	*Overlap*, %
Full, 87% overlap	1.27	4000	87
Full, 75% overlap	1.27	2000	75
Small, 75% overlap	0.64	4000	75

which are due to localized regions of lower pressure (and, consequently, lower density) inside the vortical structures. The regular vortical structures, characteristic of shear layers, are caused by an inflection instability mechanism [30]. The structures are nearly uniform in the spanwise direction. The unbiased autocorrelation functions for the forced shear layer, presented in Fig. 14a, also show that the forced shear layer has a high degree (larger than 0.6) of the correlation in the spanwise direction across the entire aperture. All of these observations suggest that the forced shear-layer wave fronts can be approximated as single-frequency spanwise-uniform wave fronts convecting at a constant speed.

The main assumption to implement the stitching method is that the flow has to be sufficiently homogeneous in the streamwise direction. In other words, the forced shear-layer growth should be minimal over the aperture. To inspect shear-layer growth over the aperture, we can treat the Shack–Hartmann measurements as a two-dimensional array of deflection angles at different spatial points. So, one way to check shear-layer growth is to study a two-dimensional map of the temporal root mean square of the deflection angles $\theta_{\text{rms}}(x, z)$ over the aperture. Figure 16a presents two-dimensional distribution of $\theta_{\text{rms}}(x, z)$ normalized by the value of θ_{rms} at the center of the aperture. Except for the first 20% of the aperture, θ_{rms} does not significantly vary along the streamwise direction. The spatial distribution of deflection angles does exhibit higher values along the middle of the aperture at $z = 0$ when compared to the locations close to the edges in the spanwise direction. This indicates a small degree of the spanwise nonuniformity; a similar conclusion was made in the previous section when analyzing the spanwise cross correlation. Another way to check the streamwise homogeneity is to inspect deflection angle spectra for various streamwise locations along $z = 0$. The plots of the deflection angle spectra for the forced shear layer at selected streamwise locations can be seen in Fig. 16b. There is a strong spectral peak at the forcing frequency of 640 Hz, as well as a weaker harmonic at 1280 Hz, present at all locations. This is indicative of a regularized structure passing over the aperture as a result of the forcing. Again, with the exception of the upstream streamwise location of $x/Ap = -0.25$, the spectral energies over a wide range of frequencies stay approximately the same at other locations of the aperture. All of it indicates that over the aperture, the flow can be treated as approximately homogeneous in the streamwise direction.

Figure 17 shows the reconstructed wave front using the full aperture set (Overlap = 87%) where several nearly spanwise-uniform large-scale structures can be clearly observed. The structures are slightly stronger along the $z = 0$ line, which is consistent with the two-dimensional map of θ_{rms} (presented in Fig. 16a) as well as with lower values of the cross-correlation function for large spanwise separations (shown in Fig. 14a). As a reminder, this

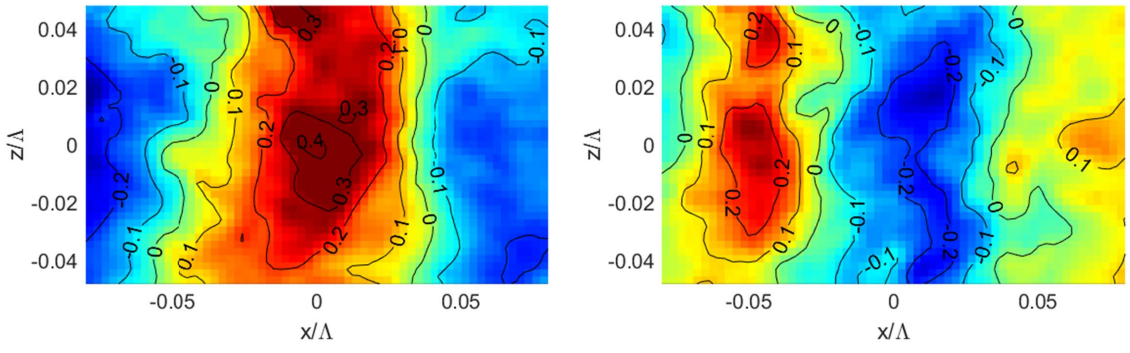

Fig. 15 Representative wave fronts for the forced shear layer. These two frames were taken at random different time instances.

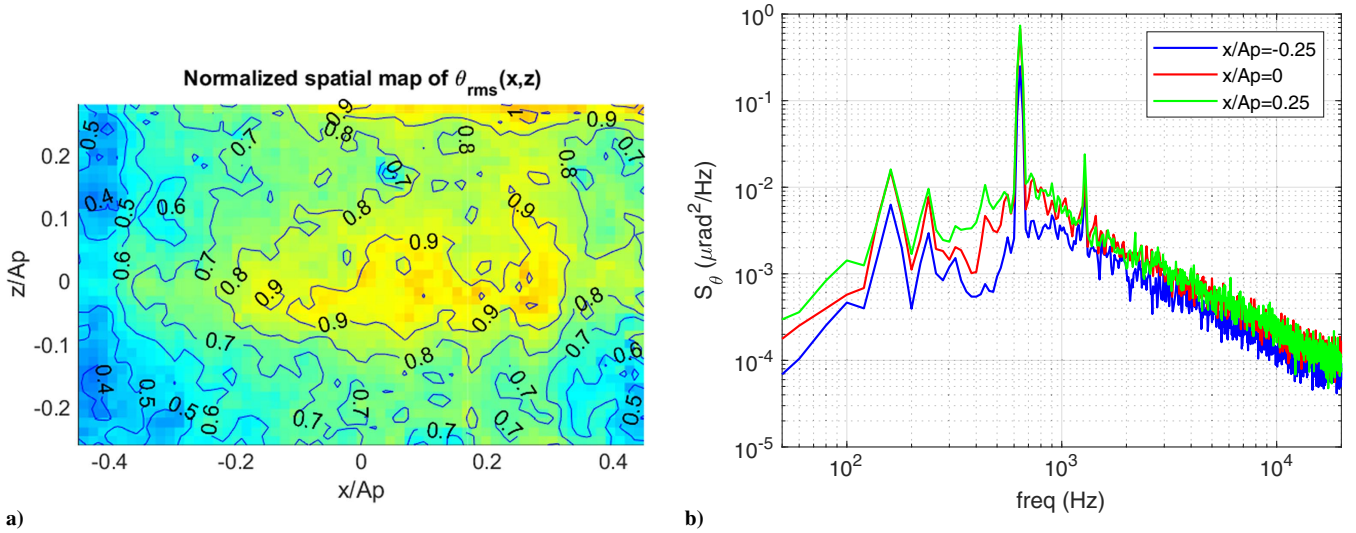

Fig. 16 Representations of a) spatial map of $\theta_{\text{rms}}(x,z)$, normalized by $\theta_{\text{rms}}(x=0,z=0)$; and b) deflection angle energy spectra of local jitter S_θ at different streamwise positions along centerline $z=0$.

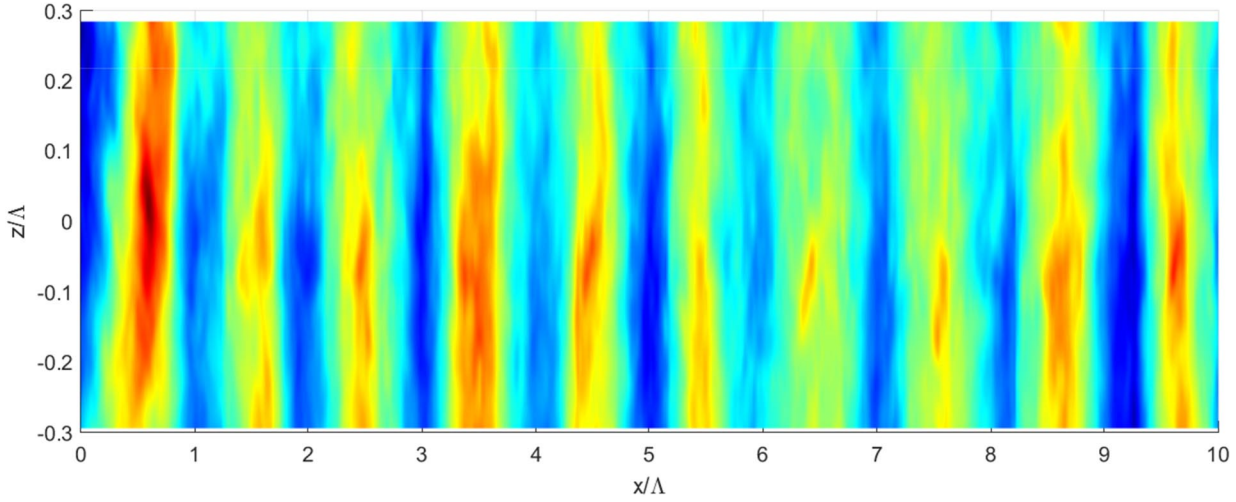

Fig. 17 Reconstructed wave front, $\tilde{W}^{\text{stitch}}(x,z)$, using the stitching method from the full aperture set (87%).

wave front was reconstructed from X/Y-tilt-removed wave fronts collected over the *fixed* aperture size of $Ap/\Lambda = 1.27$. Then, the wave front at any smaller or larger aperture can be computed. Again, the stitching method can be applied as long as the shear layer can be approximated as homogeneous in the streamwise direction. Although this approximation is reasonable for small apertures, it will eventually fail for sufficiently large apertures over which the shear-layer growth rate in the streamwise direction cannot be ignored. So, the global tilt results for large simulated apertures (to be presented later in this section) are expected to deviate from the results from the real shear layers collected over large apertures. The error analysis associated with applying the stitching method to the spatially growing flows can be found in Ref. [23].

B. Global Aero-Optical Jitter

Once the aero-optical X/Y-tilt and piston components are reintroduced into the wave fronts using the stitching method, the global tilt over any given aperture can be extracted. This is done by applying the given aperture to the reconstructed wave front, where time has been traded for space, and extracting the aero-optical only global tilt via a linear fit using Eq. (8). By moving the aperture at the constant convective speed in the streamwise direction over the reconstructed wave front, the time series of the global tilt can also be extracted, as schematically shown in Fig. 6. Note that in this work, the aperture is applied only in the streamwise direction, whereas the spanwise aperture size Ap_z stays the same.

Before presenting the results of the global tilt reconstruction via the stitching method, it is useful to develop a scaling law for the jitter. Recall that the deflection angle is a gradient of the wave front: $\boldsymbol{\theta} = -\nabla W$. If the wave front has a characteristic length scale Λ, then the amplitude of jitter characterized by the temporal root-mean-square value θ_{rms} is related to the amplitude of the wave front characterized by OPD_{rms} as $\theta_{\text{rms}} \sim \text{OPD}_{\text{rms}}/\Lambda$. In Ref. [12], it was derived that the level of aero-optical distortions for the shear layer follows this scaling law of $\text{OPD}_{\text{rms}} \sim K_{\text{GD}}\rho_\infty M_c^2 \Lambda$, where ρ_∞ denotes the freestream density and $M_c = (U_1 - U_2)/(a_1 + a_2)$ is a convective Mach number [26]. Using this equation, for the presented experiment, the convective Mach number was calculated to be $M_c = 0.24$. The freestream density was replaced with the density at the high-speed side of the shear layer to get the following scaling law for jitter:

$$\theta_{\text{rms}} \sim K_{\text{GD}}\rho_1 M_c^2 \tag{24}$$

Using this equation, we will normalize both the local jitter θ and the global tilt θ_G by $K_{\text{GD}}\rho_1 M_c^2$.

We can then move on to applying the stitching method to our forced shear-layer wave fronts and apply the variable aperture approach, as discussed earlier in this paper, to extract the aero-optical component of the global tilt for different simulated apertures. The extracted values can be used to compute various statistics of the global tilt for different simulated apertures.

Using both full aperture and small aperture sets, the normalized values of the rms of global aero-optical tilt of $\theta_{G,\mathrm{rms}}/(K_{\mathrm{GD}}\rho_1 M_c^2)$ for a range of the simulated apertures were computed and are shown in Fig. 18. The global tilt is equal to the local jitter at $Ap = 0$ and generally decreases with the increasing simulated aperture, with dropouts around $Ap/\Lambda \approx 1.4, 2.5, 3.5, 4.5$, and so on. These dropouts occur for the aperture sizes where the transfer function G_A [Eq. (7)] is equal to zero and the global tilt values are expected to significantly decrease. The results for the full aperture of 87 and 75% are nearly identical, showing the robustness of the stitching method to the *Overlap* parameter. The results for the small aperture set also agree with the results from the full aperture sets up to $Ap/\Lambda \approx 5$. Above this value, the predictions of the global tilt values from the small set become consistently below the full aperture results, although they still differ by less than a factor of two. These results are consistent with the uncertainty analysis. Also, for the small aperture set and the simulated apertures larger than $Ap/\Lambda \geq 5$, there is a small but growing mismatch between both the rms values of the global tilt and the locations of the local dropouts as compared to the full aperture results. One possible reason for this mismatch is that the stitching method relies on computing the instantaneous convective speed using the data in the overlapping region. Since the number of overlapping points is smaller for the small aperture set, the computed convective speed has a larger uncertainty, possibly resulting in this bias error in calculating the values and the dropout locations. To investigate that, the global tilt for the small aperture set was also computed by keeping the convective speed constant, and the results were found to be similar to the ones presented in Fig. 18. Further investigation is needed to address this bias error at small aperture sets. We would like to point out that this bias error is present only for the small aperture data because the large aperture does a very good job reconstructing the global jitter.

Overall, the presented results provide some guidance on the choice of the aperture size of $Ap/\Lambda \gtrsim 1$ and a number of the overlapped points $N_{\mathrm{overlap}} \gtrsim 20 - 30$ to correctly compute the values of the global tilt over a wide range of the simulated apertures. As was mentioned before, for large apertures for real flows, the assumption of the homogeneous flow over the aperture will most probably fail for most turbulent flows; and the stitching method in the presented form will provide incorrect results.

Because the forced shear layer can be approximated as a single-frequency convecting wave front, the single sine model [Eq. (21)] was able to correctly predict the values of global tilt at different simulated apertures, including the locations of the dropouts, seen in Fig. 18. The single sine model predicts the global tilt at these aperture values to be exactly zero; see Fig. 8. In reality, other frequencies present in the wave fronts will result in nonzero values of the global tilt at these dropout locations. The values of the normalized aero-optical global tilt, computed using the filter model [Eq. (20)], agree well with the values near the local maxima in the global tilt; they also correctly identify the locations of the local minima, as shown in Fig. 18. Since the filter model takes into account other frequencies present in the wave front, the values at these local minima are finite and agree reasonably well, within a factor of 1.5, with the results from the stitching method. Both models were able to correctly predict the values of the global tilt at the local maxima, which are identified as an envelope line in Fig. 18. This envelope line can be used as a conservative estimate of the global tilt values for various simulated apertures.

The extracted global tilt time series can also be used to compute global tilt energy autocorrelation spectral densities $S_G(f; Ap)$ for various simulated apertures. The results for several simulated apertures, reconstructed using both the full aperture set and the small aperture set, are shown in Fig. 19. The local jitter autocorrelation spectral density $S_\theta(f)$ is also plotted in Fig. 19 for comparison. Results are plotted as a function of the Strouhal number, based on Λ and the convective speed U_c: $St_\Lambda = f\Lambda/U_c$. All spectra have a strong peak at $St_\Lambda = 1$, corresponding to the forcing frequency. As discussed before (see Fig. 7), the aperture effect works as a low-pass filter, suppressing a contribution to the global tilt from small-scale high-frequency structures. For progressively larger apertures, the spectral energy of the global tilt is significantly reduced. As discussed before, the dropouts in the spectra correspond to the frequencies where $Z = Apf/U_c \approx 1.4, 2.5, 3.5, 4.5, \ldots$. Also, all global tilt spectra are lower than the local jitter spectrum at the low frequencies ($St_\Lambda 1$), and we will discuss this later in this paper.

The reconstructed global tilt spectra for all processed wave-front sets show a very good agreement among themselves over a wide range of frequencies. The spectra computed from the small aperture set for large ($St_\Lambda \gtrsim 5$) frequencies have slightly larger energies as compared to the ones from the full aperture sets. These results also demonstrate the ability of the stitching method to correctly reconstruct the global tilt, originally removed from the wave-front data, reasonably independently of the choice of the aperture size and the *Overlap* parameter.

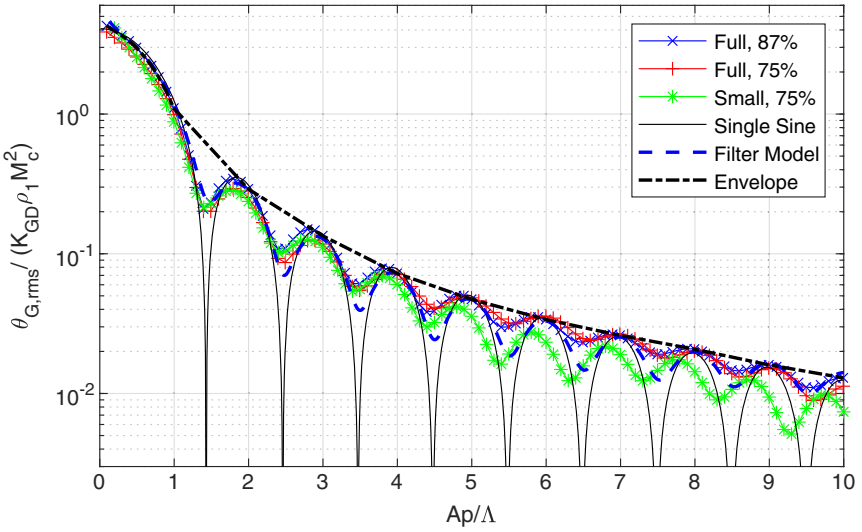

Fig. 18 $\theta_{G,\mathrm{rms}}/(K_{\mathrm{GD}}\rho_1 M_c^2)$, reconstructed from full and small aperture sets. Analytical predictions using the single sine model [Eq. (21)] and filter model [Eq. (20)] also shown for comparison.

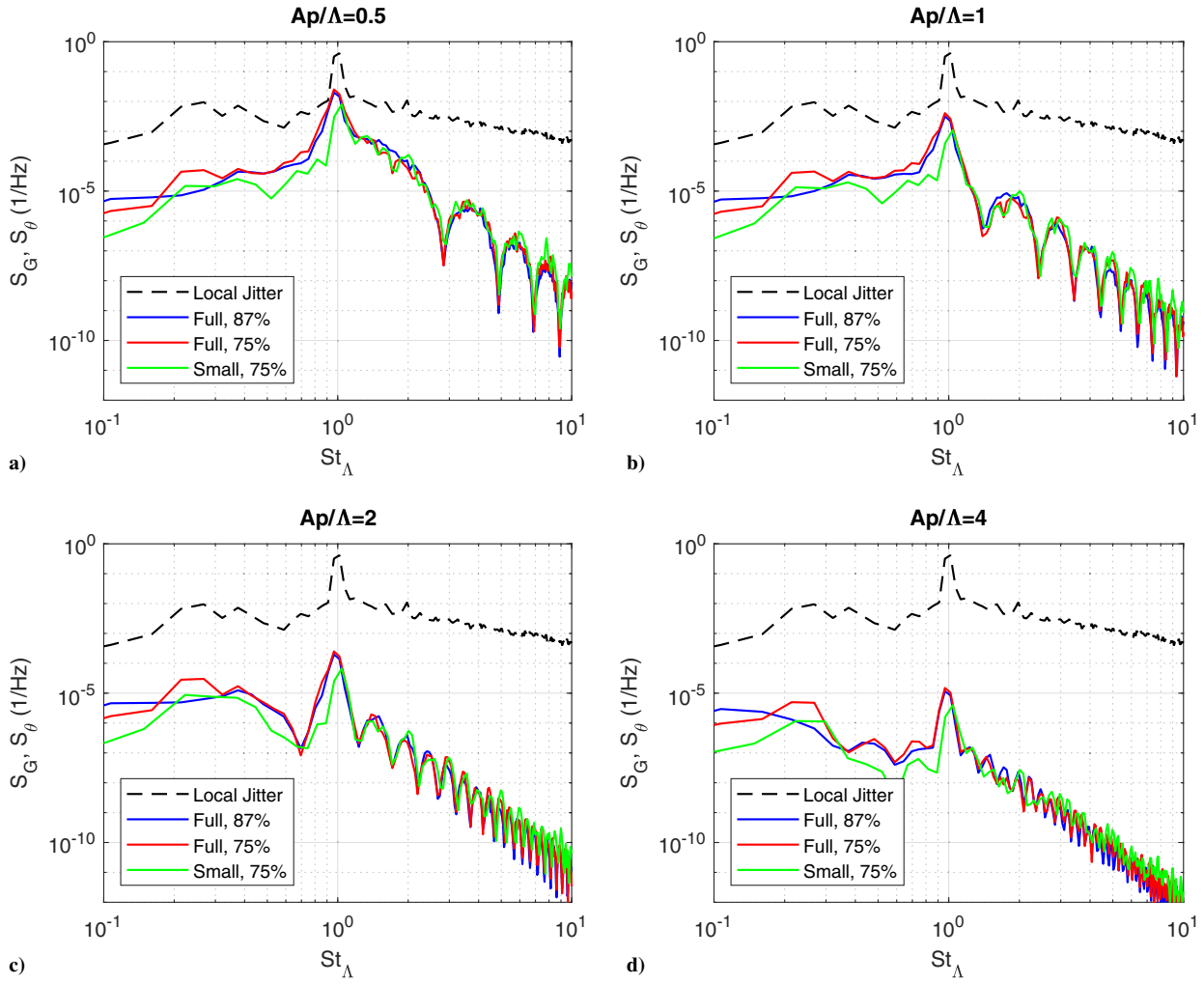

Fig. 19 Autospectral densities of normalized local jitter and global tilt calculated using stitching method from full aperture sets and small aperture set for different simulated apertures of Ap/Λ equal to a) 0.5, b) 1, c) 2, and d) 4. $St_\Lambda = f\Lambda/U_c$.

Recall that the global tilt transfer function $G_A(Z)$ given in Eq. (18) relates autocorrelation spectral densities of the local jitter and the global tilt over a given aperture; see Eq. (19). Thus, the ratio between aerocorrelation spectral densities of the global tilt and local jitter should give $S_G/S_\theta = G_A(Z)^2$. Since we have reconstructed the global tilt spectra, we can directly compute the spectral ratio and compare it with $G_A(Z)^2$. Figure 20 shows the results for several different simulated apertures computed using both the full and the small aperture sets and plotted as a function of $Z = Ap/\Lambda = (Apf)/U_c$. The filter model $G_A^2(Z)$ from Eq. (19) is also plotted for comparison. With the exception of the low frequencies ($St_{Ap}1-2$), the results match the analytical global tilt filter function quite well, including the locations of the spectral dropouts. As expected from the error analysis, the global tilt spectra at a large simulated aperture of $Ap/\Lambda = 4$ deviate more from the theoretical transfer function $G_A^2(Z)$, especially for the small aperture set. Overall, the generally good agreement between the experimentally measured spectral ratios and the filter model verifies this simple analytical model and the underlying assumptions, at least for the forced shear layer.

As noted before, the experimental spectral ratios are consistently below the analytical filter function at low frequencies. We believe the reason for this discrepancy is not related to the potential issues with the stitching method but rather with the accuracy of the measurement of the local jitter spectra. It was demonstrated in other turbulent flows, like boundary layers, that the deflection angle spectra are typically corrupted at low frequencies by mechanical vibrations and other low-frequency phenomena; see Refs. [14,31,32]. These contaminations will result in larger spectral values of the deflection angle spectra and, as a consequence, in lower values of the spectral ratio, S_G/S_θ, at low frequencies.

It should be noted once again that the filter model, which is a transfer function from the local jitter to the global tilt spectra, was able to predict the experimental results of both the global tilt spectra and overall global tilt values of tilt very well. The filter model is based on a single point measurement of the local deflection angle (jitter); so, by simply measuring the local jitter, which is unaffected by the aperture size, it is possible to develop a very good approximation for the global tilt at various apertures.

The results presented in this paper can be used to benchmark adaptive-optics systems for use in airborne directed energy platforms. For many geometries used in flight systems, a strong shear layer is typically present for looking in the downstream direction angles. The aero-optical component of the global tilt presented in this paper can be used to inform the jitter budgets developed when choosing an adaptive-optics system.

VII. Conclusions

One of the major quantities of interest for airborne laser systems is the unsteady pointing of the beam, or jitter. In airborne systems, the beam jitter is usually thought of as sourced from three components. These three components are the base motion related jitter, the aero-mechanical jitter, and the aero-optical jitter. The base motion component of the jitter is sourced primarily from vibration and unsteady motion of the platform itself. The aeromechanical component of the

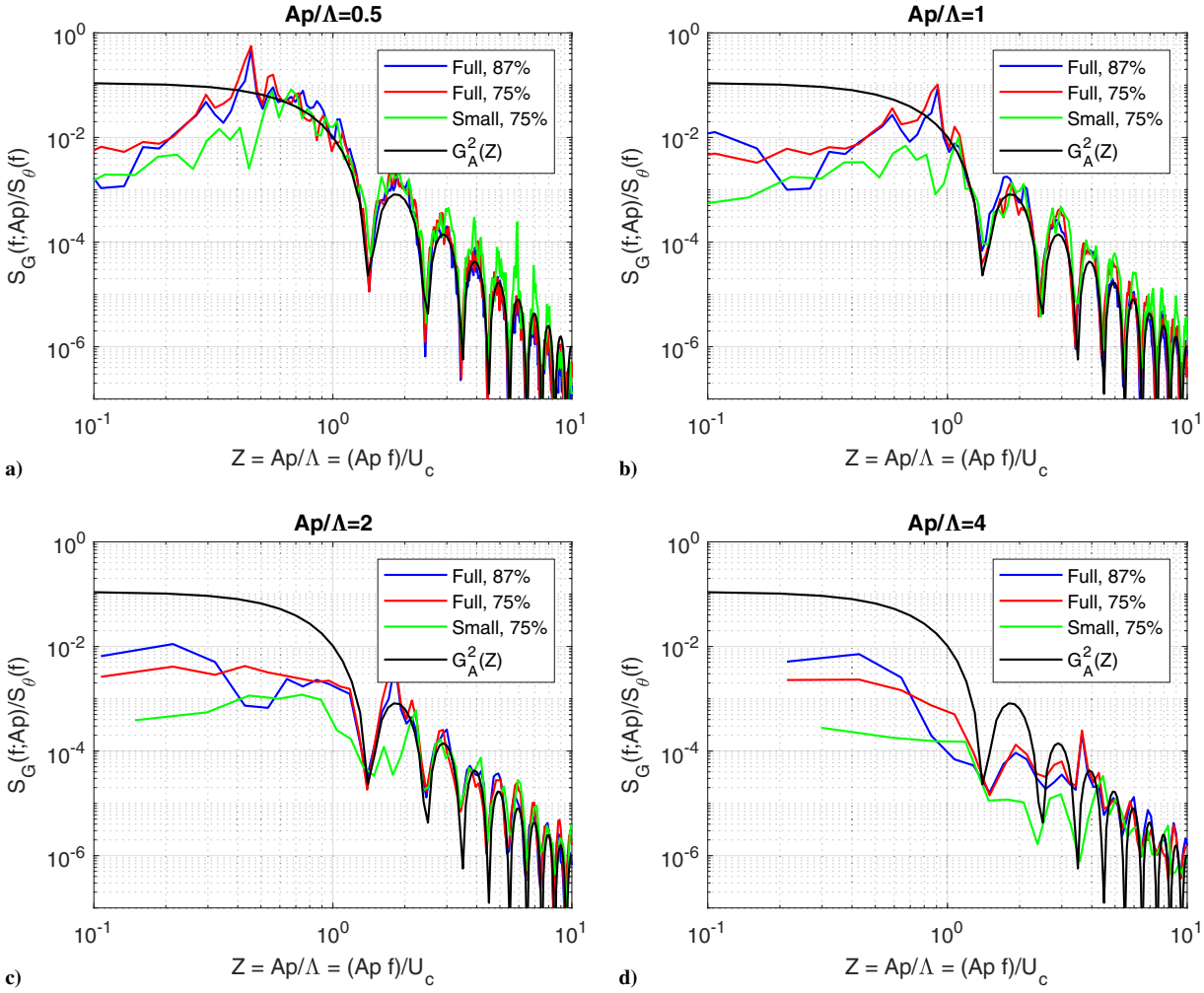

Fig. 20 Ratio between global tilt spectra and local jitter spectrum, $S_G(f;Ap)/S_\theta(f)$, calculated using data from full aperture and small aperture sets for different simulated apertures of Ap/Λ equal to a) 0.5, b) 1, c) 2, and d) 4. Filter model $G_A^2(Z)$ from Eq. (19) also plotted.

jitter results from the dynamic forcing of the beam director by the flow. The base motion-related jitter and the aeromechanical jitter can be described as being sourced from mechanical disturbances. Finally, the aero-optical component of the jitter is sourced from density variations in the flow itself. In typical experiments, it is not practically feasible to separate the mechanically sourced beam jitter from the aero-optical jitter. To compensate for the mechanical disturbances in the experiment, the three lowest-order spatial modes (X tilt, Y tilt, and piston) are commonly removed from each wave front. It is these low-order modes that are responsible for the unsteady pointing of the beam. Therefore, in the typical analysis of wave-front data, information pertaining to the aero-optical component of the jitter is lost. In this work, an algorithm was developed that takes advantage of the advective nature of aberrations to compensate for the X/Y-tilt and piston removal in the experiment. The algorithm presented in this paper and called the stitching method is able to restore information pertaining to the aero-optical component of the jitter.

The stitching method has two assumptions necessary for its application. First, the flow must be primarily convective. Second, the wave front measured must be continuous in both space and time. If wave fronts are sampled at sufficiently high frequency, there will be an overlap between frames. By measuring the X/Y tilt and the piston in the overlapped region of the consecutive wave fronts, the removed X/Y-tilt and piston components can be determined. These components can then be added back into the wave fronts to restore information pertaining to aero-optical jitter.

The stitching method presented in this work was extensively modeled. A one-dimensional sine wave with added Gaussian noise was used as a model wave front, and the stitching method was used to extract the global X tilt. It was shown that for low noise environments, the stitching method did an excellent job matching the known global jitter, with the error remaining below 25%. There are regions of large error denoted as dropouts that occur when the real global tilt of the modeled sine wave approaches zero. In addition to the error modeling, a global tilt transfer function was derived. This global tilt transfer function called the filter model relates the local jitter to the global jitter over a given aperture.

To demonstrate the stitching method, experiments were performed in Notre Dame's Tri-Sonic Wind Tunnel Facility using the shear-layer test section. The shear layer was forced using a spanwise row of voice-coil actuators mounted at the trailing edge of the splitter plate. Forcing was done to regularize the shear layer and provide a more coherent structure for the stitching algorithm. It was shown that shear-layer forcing regularized the shear layer over the aperture and generated a strong coherent shear-layer vortical structure. The stitching method along with the aforementioned filter model were applied to the forced shear-layer data to compute stitched wave fronts. Using these stitched wave fronts, the normalized jitter rms for the forced shear layer as a function of simulated aperture sizes was calculated. This normalized jitter rms matched very well with predictions from the filter model. In addition, global tilt energy spectra were computed for various simulated aperture sizes. As expected, as the aperture size increased, the overall global tilt energy decreased. Finally, the ratio between the global tilt energy and local tilt energy was calculated. This ratio serves as a direct computation of the global tilt transfer function. The ratio between the global tilt energy and the local tilt energy measured experimentally matched well with the predictions of the filter model.

Acknowledgments

This work was supported by the Directed Energy Joint Transition Office under grant no. FA9550-13-1-0001 and Office of Naval Research under grant no. N00014-18-1-2112. The U.S. Government was authorized to reproduce and distribute reprints for governmental purposes, notwithstanding any copyright notation thereon.

References

[1] Jumper, E. J., and Gordeyev, S., "Physics and Measurement of Aero-Optical Effects: Past and Present," *Annual Review of Fluid Mechanics*, Vol. 49, No. 1, 2017, pp. 419–441. https://doi.org/10.1146/annurev-fluid-010816-060315

[2] Wang, M., Mani, A., and Gordeyev, S., "Physics and Computation of Aero-Optics," *Annual Review of Fluid Mechanics*, Vol. 44, No. 1, 2012, pp. 299–321. https://doi.org/10.1146/annurev-fluid-120710-101152

[3] Gordeyev, S., and Jumper, E., "Fluid Dynamics and Aero-Optics of Turrets," *Progress in Aerospace Sciences*, Vol. 46, No. 8, 2010, pp. 388–400, http://www.sciencedirect.com/science/article/pii/S0376042110000394. https://doi.org/10.1016/j.paerosci.2010.06.001

[4] Burns, W. R., Jumper, E. J., and Gordeyev, S., "A Latency-Tolerant Architecture for Airborne Adaptive Optic Systems," *53rd AIAA Aerospace Sciences Meeting*, AIAA Paper 2015-0679, 2015. https://doi.org/10.2514/6.2015-0679

[5] Burns, W. R., "Statistical Learning Methods for Aero-Optic Wavefront Prediction and Adaptive-Optic Latency Compensation," Ph.D. Thesis, Univ. of Notre Dame, Notre Dame, IN, 2016.

[6] Gladstone, J. H., and Dale, T. P., "Researches on the Refraction, Dispersion, and Sensitiveness of Liquids," *Philosophical Transactions of the Royal Society of London*, Vol. 153, 1863, pp. 317–343, http://www.jstor.org/stable/108799.

[7] Anderson, J. H. B., "Experimental Determination of the Gladstone–Dale Constants for Dissociating Oxygen," *Physics of Fluids*, Vol. 12, No. 5, 1969, pp. I–57–I–60.

[8] Siegenthaler, J. P., "Guidelines for Adaptive-Optic Correction Based on Aperture Filtration," Ph.D. Thesis, Univ. of Notre Dame, Notre Dame, IN, 2009, https://curate.nd.edu/show/tq57np21m26.

[9] Goodman, J. W., *Introduction to Fourier Optics*, 2nd ed., Roberts and Co., Englewood, CO., 1996, p. 56.

[10] Sasiela, R. J., *Electromagnetic Wave Propagation in Turbulence Evaluation and Application of Mellin Transforms*, 2nd ed., SPIE Monograph PM171, SPIE, Bellingham, WA, 2007, p. 75.

[11] Tyson, R. K., and Frazier, B. W., *Field Guide to Adaptive Optics*, 2nd ed., SPIE Press, Bellingham, WA, 2012, p. 20.

[12] Siegenthaler, J. P., Gordeyev, S., and Jumper, E., "Shear Layers and Aperture Effects for Aero-Optics," *36th AIAA Plasmadynamics and Lasers Conference*, AIAA Paper 2005-4772, 2005.

[13] De Lucca, N., Gordeyev, S., and Jumper, E., "The Study of Aero-Optical and Mechanical Jitter for Flat Window Turrets," *50th AIAA Aerospace Sciences Meeting including the New Horizons Forum and Aerospace Exposition*, AIAA Paper 2012-0623, 2012. https://doi.org/10.2514/6.2012-623

[14] Gordeyev, S., Smith, A. E., Cress, J. A., and Jumper, E. J., "Experimental Studies of Aero-Optical Properties of Subsonic Turbulent Boundary Layers," *Journal of Fluid Mechanics*, Vol. 740, 2014, pp. 214–253.

[15] De Lucca, N. G., "Studies of the Pressure Field and Related Beam Jitter for Hemisphere-on-Cylinder Turrets," Ph.D. Thesis, Univ. of Notre Dame, Notre Dame, IN, 2016.

[16] Smith, A. E., "Evaluation of Passive Boundary Layer Flow Control Techniques for Aero-Optic Mitigation," Ph.D. Thesis, Univ. of Notre Dame, Notre Dame, IN, 2015.

[17] Smith, A., Gordeyev, S., and Jumper, E., "Aperture Effects on Aero-Optical Distortions Caused by Subsonic Boundary Layers," *43rd AIAA Plasmadynamics and Lasers Conference 2012*, AIAA Paper 2012-2986, 2012.

[18] Taylor, G. I., "The Spectrum of Turbulence," *Proceedings of the Royal Society of London, Series A: Mathematical and Physical Sciences*, Vol. 164, No. 919, 1938, pp. 476–490.

[19] Morrida, J., Gordeyev, S., De Lucca, N., and Jumper, E. J., "Shock-Related Effects on Aero-Optical Environment for Hemisphere-on-Cylinder Turrets at Transonic Speeds," *Applied Optics*, Vol. 56, No. 16, 2017, pp. 4814–4824. https://doi.org/10.1364/AO.56.004814

[20] Venema, T. M., and Schmidt, J. D., "Optical Phase Unwrapping in the Presence of Branch Points," *Optics Express*, Vol. 16, No. 10, 2008, pp. 6985–6998.

[21] Fried, D. L., and Vaughn, J. L., "Branch Cuts in the Phase Function," *Applied Optics*, Vol. 31, No. 15, 1992, pp. 2865–2882.

[22] Fried, D., "Branch Point Problem in Adaptive Optics," *Journal of the Optical Society of America A: Optics and Image Science, and Vision*, Vol. 15, No. 10, 1998, pp. 2759–2768.

[23] Kemnetz, M. R., "Analysis of the Aero-Optical Component of the Jitter Using the Stitching Method," Ph.D. Thesis, Univ. of Notre Dame, Notre Dame, IN, 2019, https://curate.nd.edu/show/k930bv76j74.

[24] Wang, K., and Wang, M., "Aero-Optics of Subsonic Turbulent Boundary Layers," *Journal of Fluid Mechanics*, Vol. 696, 2012, pp. 122–151.

[25] Gordeyev, S., Jumper, E., and Hayden, T. E., "Aero-Optical Effects of Supersonic Boundary Layers," *AIAA Journal*, Vol. 50, No. 3, 2012, pp. 682–690.

[26] Papamoschou, D., and Roshko, A., "The Compressible Turbulent Shear Layer: An Experimental Study," *Journal of Fluid Mechanics*, Vol. 197, 1988, pp. 453–477.

[27] Freeman, J. L., "On the Growth Rate of Turbulent Mixing Layers: A New Parametric Model," M.S. Thesis, California Polytechnic State Univ., San Luis Obispo, CA, 2014.

[28] Duffin, D. A., "Feed-Forward Adaptive-Optic Correction of a Weakly-Compressible High-Subsonic Shear Layer," Ph.D. Thesis, Univ. of Notre Dame, Notre Dame, IN, 2009, https://curate.nd.edu/show/0v838051762.

[29] Ranade, P. M., "Turbulence Amplitude Modulation in an Externally Forced, High Reynolds Number Boundary Layer," Ph.D. Thesis, Univ. of Notre Dame, Notre Dame, IN, 2016, https://curate.nd.edu/show/gt54kk93q36.

[30] Fitzgerald, E. J., and Jumper, E. J., "The Optical Distortion Mechanism in a Nearly Incompressible Free Shear Layer," *Journal of Fluid Mechanics*, Vol. 512, 2004, pp. 153–189.

[31] Smith, A. E., Gordeyev, S., Ahmed, H., Ahmed, A., and Wittich, D. J., "Shack-Hartmann Wavefront Measurements of Supersonic Turbulent Boundary Layers in the TGF," *45th AIAA Plasmadynamics and Lasers Conference*, AIAA Paper 2014-2493, 2014. https://doi.org/10.2514/6.2014-2493

[32] Gordeyev, S., and Juliano, T. J., "Optical Characterization of Nozzle-Wall Mach-6 Boundary Layers," *54th AIAA Aerospace Sciences Meeting*, AIAA Paper 2016-1586, 2016. https://doi.org/10.2514/6.2016-1586

L. Ukeiley
Associate Editor